Orbital- and Millennial-Scale Variability in Northwest African Dust Emissions Over the Past 67,000 years

Christopher W. Kinsley[1], Louisa I. Bradtmiller[2], David McGee[1], Michael Galgay[2], Jan-Berend Stuut[3,4], Rik Tjallingii[5], Gisela Winckler[6], and Peter B. deMenocal[6]

[1]Department of Earth, Atmospheric and Planetary Sciences, Massachusetts Institute of Technology, Cambridge, MA, USA, [2]Department of Environmental Studies, Macalester College, St. Paul, MN, USA, [3]NIOZ Royal Netherlands Institute for Sea Research, Texel, The Netherlands, [4]Faculty of Science, Department of Earth Sciences, Vrije Universiteit Amsterdam, Amsterdam, The Netherlands, [5]GFZ German Research Centre for Geosciences, Section 'Climate Dynamics and Landscape Evolution', Potsdam, Germany, [6]Lamont-Doherty Earth Observatory, Columbia University, Palisades, NY, USA

Corresponding author: Christopher W. Kinsley (ckinsley@mit.edu)

Key Points:

- Coherent dust flux changes along the NW African margin and in the central North Atlantic over the last 67 ka
- Abrupt dust flux variations on millennial timescales similar to N Atlantic stadials related to high latitude forcing of African climate
- Green Sahara interval (60-50 ka) recorded by low dust fluxes to ODP 658C showing an orbitally-forced strengthening of monsoon during MIS 3

Abstract

Reconstructions of aeolian dust flux to West African margin sediments can be used to explore changing atmospheric circulation and hydroclimate over North Africa on millennial to orbital timescales. Here, we extend West African margin dust flux records back to 35 ka in a transect of core sites from 19°N to 27°N, and back to 67 ka at Ocean Drilling Program (ODP) Hole 658C, in order to explore the interplay of orbital and high-latitude forcings on North African climate and make quantitative estimates of dust flux during the core of the Last Glacial Maximum (LGM). The ODP 658C record shows a "Green Sahara" interval from 60 to 50 ka during a time of high Northern Hemisphere summer insolation, with dust fluxes similar to levels during the early Holocene African Humid Period, and an abrupt peak in flux during Heinrich event 5a (H5a). Dust fluxes increase from 60 to 35 ka while the high-latitude Northern Hemisphere cools, with peaks in dust flux associated with North Atlantic cool events. From 35 ka through the LGM dust deposition decreases in all cores, and little response is observed to low-latitude insolation changes. Dust fluxes at sites north of 20°N were near late Holocene levels during the LGM time slice, suggesting a more muted LGM response than observed in mid-latitude dust sources. Records along the northwest African margin suggest important differences in wind responses during different stadials, with maximum dust flux anomalies centered south of 20°N during H1 and north of 20°N during the Younger Dryas.

1 Introduction

Records of mineral dust emissions from the Sahara Desert are essential for understanding past changes in North African climate, and are tightly linked to the strength of the West African monsoon (deMenocal, 1995; deMenocal, et al., 2000; Skonieczny et al., 2019; Wang, et al., 2015). Wind speed and aridity variations are expressed as fluctuations in the amount of dust exported from the North African continent to the Atlantic Ocean, meaning that downcore measurement of dust flux to North Atlantic sediments allows an integrated reconstruction of how winds and aridity respond to climate changes.

In the present day, North African dust outbreak events transport dust over the northwest African continental margin and Atlantic Ocean throughout the year. Observational records from marine sediment traps and atmospheric dust samplers suggest that maximum dust deposition along the northwest African margin occurs in winter and spring (Bory & Newton, 2000;

Chiapello et al., 1995; Ratmeyer et al., 1999; Skonieczny et al., 2013). Combining air parcel back trajectory modeling with dust provenance (Friese et al., 2017; Skonieczny et al., 2013) and grain size measurements (van der Does et al., 2016) suggests that winter dust is transported in low-level trade winds from relatively proximal locations, including the coastal region of Western Sahara and western Mauritania (see Scheuvens et al., 2013 for a compilation of PSA locations). Interannual peaks in winter dust emissions are attributed to southward movement of the ITCZ and increased surface winds over North African dust source regions, with a minor role of reduced Sahel rainfall (Doherty et al., 2012).

During summer, dust is transported from source regions closer to the center of the continent (e.g., Libya) and uplifted at the coast by a cool marine inversion layer and transported by the upper level (~1.5-4.5 km) Saharan Air Layer (Carlson & Prospero, 1972). Satellite observations of atmospheric dust loading and fluxes show peak dust transport across the Atlantic in summer (Ridley et al., 2012; Yu et al., 2015); however, relatively little of this dust appears to be deposited on the northwest African margin (Skonieczny et al., 2013). As a result, our records are likely to be biased toward winter dust emissions from the western Sahara Desert. To address this potential seasonal and spatial bias in our interpretations, in section 4.1 we compare data from our African margin sites with data from a distal core site that represents predominantly summer dust deposition from interior African source regions (Middleton et al., 2018).

Paleoclimate proxy records and geochemical tools have been used to extend the record of variability of dust transport to the margin beyond the observational record, which exists only from the mid-1960s (Prospero & Lamb, 2003). Records of the last 20 ka (ka: thousand years before present) were developed using sediments from Ocean Drilling Program (ODP) Hole 658C by deMenocal et al. (2000) and Adkins et al. (2006). Later work demonstrated that the variations in this core were coherent along the northwest African margin between 19°N and 27°N (McGee et al., 2013) and were observed across the Atlantic Basin in the Bahamas and central Atlantic as well (Williams et al., 2016). These reconstructions show an abrupt transition from a time of high dust accumulation during the deglaciation to a sustained period of low dust accumulation between 12 and 5 ka. This low-dust period is known as the African Humid Period (AHP) and is marked by an abrupt onset and termination, followed by a more gradual increase of dust accumulation toward the present. Comparison of these dust records with other climate proxy records of North African climate shows that the AHP marks a “Green Sahara”, when the Sahara

Desert received high rainfall supporting diverse and widespread vegetation, permanent lakes, and human populations (McGee & deMenocal, 2017, and references therein), with accompanying continental runoff (Drake et al., 2010; Skonieczny et al., 2015; Weldeab et al., 2014). The AHP occurred when Northern Hemisphere summer insolation was increased relative to the present due to precessional variation, which has been shown through modeling efforts to increase the extent and intensity of the monsoon system (Battisti etal., 2014; Braconnot et al., 2012; Kutzbach, 1981; Tjallingii et al., 2008). There is also evidence that trade wind strength was decreased over the West African margin during the AHP, as evidenced by decreased upwelling-related biogenic fluxes to margin sediments and increased sea surface temperatures (SSTs) along the margin (Adkins et al., 2006; Bradtmiller et al., 2016). These findings over the AHP highlight two of the controls on changes to dust flux from North Africa, aridity and wind strength, and the importance of considering the interplay between the two.

These studies also began to elucidate dramatic intervals of rapid and high-amplitude changes to climate and dust transport in this region over far shorter timescales, punctuating the orbitally-forced record at a millennial scale. During abrupt Northern Hemisphere cooling events such as Heinrich event 1 (H1) (~18.0 to 15 ka), and the Younger Dryas (YD) episode (12.8 to 11.7 ka; Rasmussen et al., 2006) abrupt increases in dust flux have been recorded at multiple sites over the margin, with fluxes reaching the highest values of their respective records during these events (Adkins et al., 2006; McGee et al., 2013; Mulitza et al., 2008).

Multiple studies have linked North Atlantic cooling to increases in northeasterly winds over North Africa (deMenocal et al., 1993; McGee et al., 2018; Meyer et al., 2013; Mulitza et al., 2008; Tjallingii et al., 2008). Cooling of winter SSTs and expansion of sea ice in the North Atlantic shift the Atlantic ITCZ to the south, weakening the monsoon and increasing trade wind strength, leading to an increase of dust export (Liu et al., 2014; Murphy et al., 2014). Consistent with this finding from models, northwest African margin sediments record increases in the accumulation of biogenic opal and organic carbon during these cold events, suggesting increased wind-driven upwelling (Adkins et al., 2006; Bradtmiller et al., 2016; Romero et al., 2008). A weakening of monsoon rainfall during North Atlantic cooling events also shifts the Sahel-Sahara boundary south (Collins et al., 2013), potentially opening up new dust source areas and further contributing to the increase in dust emissions during these events. These high-resolution studies provide evidence for a North Atlantic high-latitude control causing abrupt changes to

atmospheric circulation and North African climate on millennial timescales, in addition to the low-latitude orbital regulation of African monsoonal climate.

Recent efforts by Skonieczny et al. (2019) have shown a high correlation of Saharan dust flux, calculated using ^{230}Th normalization, with summer insolation over the last 240 ka, confirming low-latitude pacing of northwest African dust fluxes at 18°N spanning at least the last two glacial cycles for sediment core MD03-2705. Low sedimentation rates for core MD03-2705, which is adjacent to ODP Hole 658C, precluded detailed study of potential millennial scale controls on North African climate over this longer time frame. Here we present northwest African margin dust flux records from core sites with higher sedimentation rates (5-10 cm kyr^{-1}) to explore the combined effects of high-latitude and orbital forcing of African climate extending back to 67 ka. Probing this time period allows us to examine over multiple precessional cycles the impact of high-latitude and summer insolation forcing on dust export, and to provide quantitative estimates of dust flux during the core of the LGM time slice. We also explore how millennial-scale increases in dust emission varied along a north-south transect of cores, providing insight into the spatial distribution of wind and aridity changes during these events. Drawing on the mechanistic links between regional climate and dust export, we aim to deepen understanding of changing climate of the North Africa region over the past 67 ka.

2 Methods and Core Sites

2.1 Core Locations

A meridional transect of 4 core sites between 27°N and 19°N were used in this study (Figure 1). These sites have been used to monitor past variations in northwest African climate (Bradtmiller et al., 2016; McGee et al., 2013; Williams et al., 2016), as they represent North African dust emissions to the tropical North Atlantic. The southernmost core lies on the northern edge of the modern day winter dust plume (e.g., Mulitza et al., 2008; Skonieczny et al., 2019; Yu et al., 2015) meaning the sites are sensitive to latitudinal variations in dust export. The three gravity cores GC37, GC49, and GC68, were taken by the R/V Oceanus during the 2007 Changing Holocene Environments of the Eastern Tropical Atlantic (CHEETA) cruise (OC437-7). The sediments from Ocean Drilling Program Hole 658C off Cap Blanc, Mauritania were cored during ODP Leg 108 (Ruddiman et al., 1988).

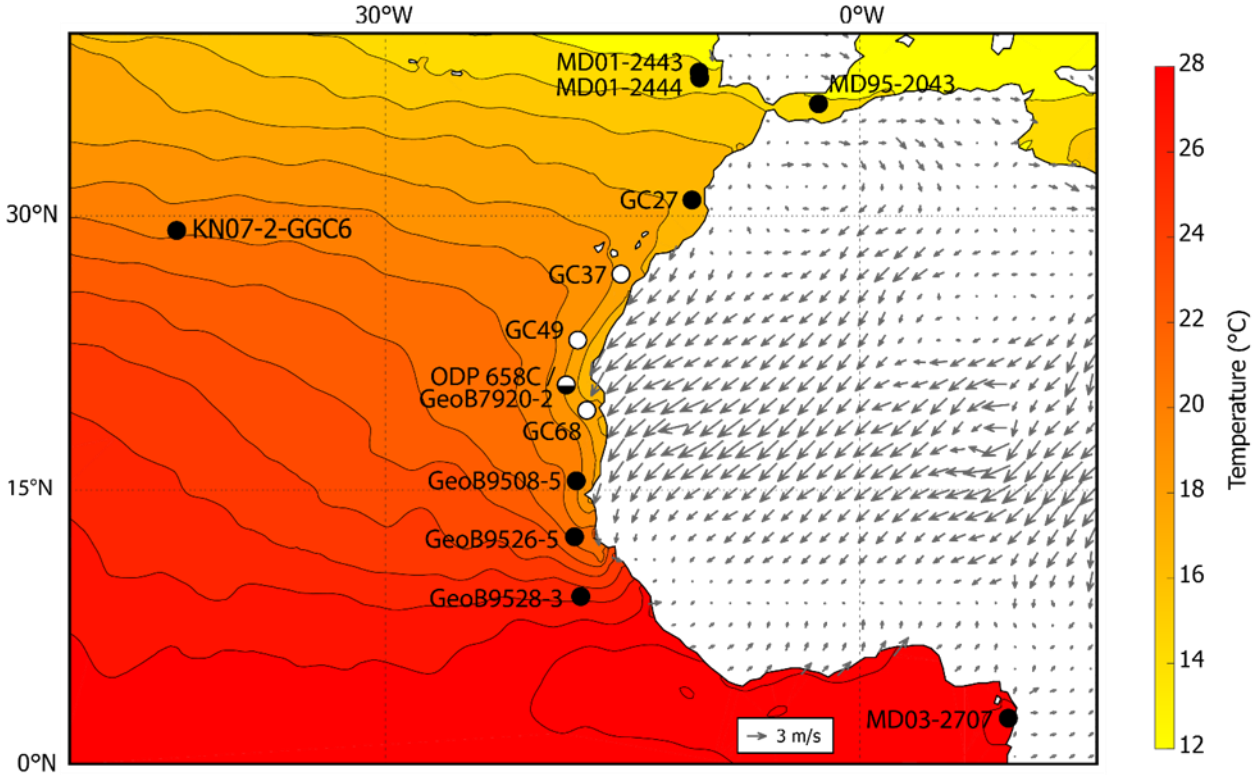

Figure 1. Map showing studied core sites (white circles) and referenced core sites (black circles), JFM SSTs from the WOA18 (black contours; Locarnini et al., 2019), and ERA5 10m JFM winds (grey arrows; C3S, 2017). Studied core locations and water depths as follows: GC37 (26°48.96'N, 15°7.06'W, 2771 m), GC49 (23°12.37'N, 17°51.25'W, 2303 m), ODP 658C (20°44.95'N, 18°34.85'W, 2263.6 m), GC68 (19°21.78'N, 17°16.94'W, 1396 m).

2.2 Age Models

The chronologies for the OC437-7 cores were developed from AMS radiocarbon ages on planktonic foraminifera (see Supplementary Information Figure S1). Radiocarbon ages younger than 20 ka in GC37 and GC68 and ages as old as 31.5 ka in GC49 were taken from McGee et al. (2013). Seven new radiocarbon ages were measured for this study (see Supplementary Information S1). The ages for this study were determined on specimens of *Globigerina bulloides*; radiocarbon measurements were performed at the Center for Accelerator Mass Spectrometry at Lawrence Livermore National Laboratory. Radiocarbon ages were converted to calendar ages using Marine13 (Reimer et al., 2013), with an additional reservoir correction (ΔR)

of 130 ± 50 yr (2σ) based upon local modern reservoir ages (Mulitza et al., 2010; Ndeye, 2008; Pittauerov et al., 2009). We do not attempt to estimate past changes in reservoir age, though these most certainly accompanied the dramatic changes in upwelling observed in African margin records (Bradtmiller et al., 2016; Romero et al., 2008). Age models were interpolated between ^{14}C tie points using the P_Sequence routine in OxCal 4.2 (Bronk Ramsey, 2008). This routine provides Bayesian age-depth modeling and treats sediment deposition as a series of discrete "events" following a Poisson distribution with a user-specified step size. A step size (k) of 0.75 cm^{-1} provided sufficient flexibility in the age-depth relationship to fit our ^{14}C ages.

The chronology for the ODP 658C core is based on AMS radiocarbon ages and correlation to a geochemical record from a nearby core with existing age model (see Supplementary Information Figure S2). From 20 ka to the coretop radiocarbon ages from deMenocal et al. (2000) are utilized, and two new radiocarbon ages determined on specimens of *Globigerina bulloides* were measured for this study to constrain the chronology from 38.5 to 30 ka. Radiocarbon ages were calibrated using Marine13 and a constant ΔR of 130 years. Between 67 ka and 25 ka the chronology is based on matching $CaCO_3$ weight percent in ODP 658C to calibrated XRF $CaCO_3$ weight percent in neighboring core GeoB7920-2 (see Supplementary Information Figure S3). The age model for this part of GeoB7920-2 is based on visual correlation of the benthic (*Cibicidoides wuellerstorfi*) $\delta^{18}O$ record with that of marine sediment core MD95-2042, with the $\delta^{18}O$ stratigraphy of MD95-2042 on the GRIP ss09sea age scale (Tjallingii et al., 2008).

2.3 Determination of Biogenic Components and Aeolian Fraction of Sediments

The detrital percentage of the samples was calculated as the residual after subtracting the carbonate, opal and organic carbon percentages measured at Macalester College. Percent carbonate and percent total carbon were determined through coulometry. Percent organic carbon was calculated as the difference between total carbon and carbonate carbon. Percent biogenic opal was determined using alkaline extraction and molybdate blue spectrophotometry after the method of Mortlock & Froelich (1989).

The aeolian fraction of the sediments was calculated by measuring grain size and utilizing endmember modeling of grain size distributions to sum the two coarsest endmembers, which are taken to represent the aeolian fraction of the detrital material, as determined above.

This approach derives from multiple studies showing that the grain size distributions of northwest African margin can be approximated well by three endmembers (Holz et al., 2004, 2007; McGee et al., 2013; Mulitza et al., 2008; Tjallingii et al., 2008); that the two coarser endmembers are similar in grain size to modern-day dust collected by dust traps (Stuut et al., 2005); and that the finest endmember peaks in abundance near river mouths (Holz et al., 2004) and varies in flux independently from the other two endmembers (McGee et al., 2013). Prior to grain size measurement the non-detrital fraction of the sediment was removed in a stepwise leaching procedure. Organic matter and calcium carbonate were removed in a glass beaker using excess 10% hydrogen peroxide and 0.1 M hydrochloric acid, respectively. Opal was removed by transferring the samples to centrifuge tubes, adding excess 2 M sodium carbonate, and heating the samples in an 80°C hot bath for 5 hours. Grain size measurements were made on a Beckman Coulter LS 13320 Laser Diffraction Particle Size Analyzer at the Royal Netherlands Institute for Sea Research.

The grain size distribution below 250 μm was used for grain size endmember modelling in order to separate aeolian from hemipelagic inputs. The grain size data for each core was fit using Weibull distributions, which are unimodal, asymmetric distributions that closely approximate measured grain size distributions of airborne dust and loess (Sun, 2004; Zobeck et al., 1999). Three endmembers per core were used to model the grain size distributions, with the two coarsest endmembers identified as aeolian dust, following the work of McGee et al. (2013). The proportion of the grain size distribution that is accounted for by the two coarsest endmembers was taken as the fraction of the detrital material that is aeolian, and this value was multiplied by the detrital percentage to obtain the aeolian fraction of the bulk sediments.

The same endmember distributions that McGee et al., (2013) calculated for cores GC37, GC49, and GC68 were utilized to estimate aeolian fractions for new sediment samples in this study for those sites. For core ODP 658C best fit endmember distributions were calculated from grain size distribution data on all samples analyzed in this study (from 67 to 18.8 ka), and used to estimate the aeolian fraction of the bulk sediments (see Supplementary Information S3 and Figure S4).

231 2.4 U, Th Isotope Measurements

232 Aeolian fluxes were calculated by multiplying the aeolian fraction of the sediments by
233 the vertical sediment flux. Sediment fluxes were calculated using $^{230}Th_{xs}$-normalization (Bacon,
234 1984; Suman & Bacon, 1989), which utilizes the fact that the instantaneous ratio of water
235 column scavenged ^{230}Th flux to the total sediment flux must be equal to the concentration of
236 ^{230}Th in the underlying sediment:
237

$$\text{normalized aeolian flux} = \frac{\beta z}{[^{230}Th_{xs}^{0}]} F$$

238
239 (Equation 1)
240
241 where β is the production rate of ^{230}Th from ^{234}U in the water column (0.0268 dpm m^{-3} yr^{-1}, McGee et al., 2010), z is the water column depth (m), $[^{230}Th_{xs}{}^{0}]$ is the concentration of the
243 component of the total $^{230}Th_{meas}$ that is not derived from detrital material or supported by ^{238}U
244 decay within the sediments (in dpm/g), and has been corrected for decay since it was deposited,
245 and F is the fraction of aeolian material. The water column depth was adjusted for changing sea
246 level (Waelbroeck et al., 2002) as this affects the production rate of ^{230}Th in the water column.
247 $^{230}Th_{xs}{}^{0}$ is calculated using the following equation:
248

$$^{230}Th_{xs}^{0} = e^{\lambda_{230} t} \times \left[{}^{230}Th_{meas} - {}^{230}Th_{det} - {}^{230}Th_{auth} \right]$$

249
250 (Equation 2)
251
252 The correction for decay was made using the age model of the core to assign an age to
253 each sample and account for the decay of initial excess $^{230}Th_{xs}$ since the time of deposition. The
254 detrital ^{230}Th was calculated by assuming the ^{232}Th content of the sample was entirely sourced
255 from the detrital component, and calculating the activity of the ^{238}U associated with this detrital
256 component using an estimated detrital $^{238}U/^{232}Th$ activity ratio of 0.7 ± 0.05 (1σ) for this area
257 (Adkins et al., 2006). The detrital ^{230}Th is assumed to be in secular equilibrium with this
258 uranium, so it can be subtracted from the $^{230}Th_{meas}$. Authigenic uranium is taken to be that which

remains after accounting for the detrital uranium. Authigenic ^{230}Th is therefore calculated by assuming that the formation of authigenic minerals/coatings occurs at the time of sediment deposition and incorporates ^{234}U/^{238}U at a constant seawater activity ratio of 1.1468 (Andersen et al., 2010).

In preparation for isotopic measurements samples were weighed, doped with a mixed spike of ^{229}Th and ^{236}U, and fully dissolved with hydrogen peroxide, nitric acid, hydrochloric acid and hydrofluoric acid. An iron coprecipitation step allowed removal of much of the matrix of the dissolved sediments and thus improved yields of Th and U. Samples then underwent anion exchange chromatography using Dowex Bio-Rad AG1-X8 100-200 mesh anion exchange resin to separate Th and U so that the two elements could be measured separately. ^{230}Th, ^{232}Th, and ^{238}U isotope measurements were made using a multi-collector inductively coupled plasma source mass spectrometer (MC-ICP-MS). The majority of isotopic measurements were made using a ThermoScientific Neptune Plus MC-ICP-MS at Brown University; more recent measurements were made on a Nu Plasma II-ES MC-ICP-MS at MIT.

Uncertainties in the final aeolian fluxes reported reflect confidence limits associated with mass spectrometric measurements, the detrital U/Th ratio, and the aeolian fraction of the sediments. The uncertainties in aeolian fluxes do not incorporate uncertainties in the assumption that the supply of scavenged ^{230}Th to the sediment is equivalent to the production rate of ^{230}Th in the overlying water column. Our core sites lie in an exceptionally productive region of upwelling which can lead to boundary scavenging of ^{230}Th: there is strong year round upwelling from 20 to 26°N along the West African margin, with weaker year round upwelling north of 26°N, and seasonal upwelling south of 20°N (Gómez-Letona et al., 2017). Currently, boundary scavenging of ^{230}Th has been constrained to 40 ± 10% of its water column production off northwest Africa (Hayes et al., 2015), helping to quantify this additional uncertainty associated with ^{230}Th-normalized sediment fluxes in our study region. This scavenging would increase ^{230}Th deposition in sediments at our core sites, biasing our accumulation rates low. It is assumed that changes in anomalous ^{230}Th deposition due to changes in boundary scavenging are much smaller than the factor of >3 changes in aeolian flux seen in our records, meaning that relative changes in flux are likely to be robust even if the mean flux is biased low.

3 Results

The meridional sediment core transect along the northwest African margin reveals latitudinal differences in the relative expressions of low-latitude (orbital monsoon) and high-latitude (glacial and stadial event) forcing on regional dust fluxes and coastal upwelling (Figure 2). Dust, opal, and organic carbon fluxes for the 20 ka to coretop portions of GC37, GC49 and GC68 were previously published in McGee et al., (2013) and Bradtmiller et al., (2016), respectively. Carbonate, opal, and detrital fluxes for the 20 ka to coretop portion of ODP 658C were previously published in Adkins et al., (2006).

3.1 GC37 (27°N)

Dust fluxes in core GC37 exhibit a maximum from 36 to 31 ka during late marine isotope stage (MIS) 3 (~0.5 g cm^{-2} kyr^{-1}), with a millennial-scale peak coincident with H3 (31.3 ka) (Sánchez Goñi & Harrison, 2010). Fluxes gradually fall during MIS 2 to moderately low values (0.26 g cm^{-2} kyr^{-1}) in the late LGM (~20 ka), with a small dust peak associated with H2 (24 ka). Dust fluxes rise to millennial-scale peaks during H1 (0.37 g cm^{-2} kyr^{-1}) and the YD (0.47 g cm^{-2} kyr^{-1}), with the YD showing a 20% higher peak flux of dust than H1. Fluxes abruptly fall during the onset of the AHP at ~12 ka, and continue to fall to the lowest recorded value at ~6 ka (0.09 g cm^{-2} kyr^{-1}). Dust fluxes then increase into the Late Holocene (~1 ka) to a value of ~0.2 g cm^{-2} kyr^{-1}.

Both opal and organic carbon fluxes are highly correlated with dust fluxes in core GC37 ($r^2 = 0.69$; p-value < 0.05 and $r^2 = 0.43$; p-value < 0.05, respectively). Similar to dust, both opal and organic carbon are at maximum levels at ~36 ka, the base of the core. Biogenic fluxes decrease into the LGM, with opal more closely tracking dust and organic carbon dropping rapidly after 30 ka. Opal fluxes rise to high levels during both H1 and the YD, while organic carbon fluxes peak only in H1. Fluxes of both opal and organic carbon fall to low levels throughout the AHP before rising during the late Holocene.

3.2 GC49 (23°N)

Dust fluxes in core GC49 decrease steadily from a late MIS 3 maximum at 36 ka (0.74 g cm^{-2} kyr^{-1}) to moderately low values during the late LGM at ~21 ka (0.52 g cm^{-2} kyr^{-1}), with a small peak coincident with H2 (24 ka). Dust fluxes then rise to peaks during H1 (0.65 g cm^{-2} kyr^{-}

$^{-1}$) and the YD (0.84 g cm^{-2} kyr^{-1}), before decreasing to a minimum during the AHP (0.076-0.11 g cm^{-2} kyr^{-1}). Similar to the GC37 record, the dust flux peak associated with the YD is larger – by ~30% – than the H1 peak, showing a stronger dust response during the YD in the northern core sites. Dust fluxes then increase into the Late Holocene to a value of 0.52 g cm^{-2} kyr^{-1}.

Both opal and organic carbon fluxes are highly correlated with dust fluxes in core GC49 ($r^2 = 0.45$; p-value < 0.05 and $r^2 = 0.39$; p-value < 0.05, respectively). Opal and organic carbon fluxes are at high levels during late MIS 3 at ~36 ka, the end of the core, and both decrease into the LGM. Opal fluxes more closely track dust fluxes, also showing a peak coincident with H2 (24 ka), while the organic carbon fluxes drop rapidly after 30 ka and are highly variable during the early part of the LGM. Opal fluxes rise to high levels during H1 and the YD, while organic carbon fluxes peak only in H1 and show an earlier peak from 21-18 ka at the end of the LGM. Fluxes of both opal and organic carbon fall to low levels throughout the AHP before rising during the late Holocene.

3.3 GC68 (19°N)

Core GC68 provides the highest resolution dust fluxes in this study due to the high sediment accumulation rates at this site, which is the closest site in the transect to the core of the Saharan dust plume. The highest sedimentation rates are in the older portion of the core, from 26 to 13 ka, at a time when the dust fraction of the material averages 80 to 90 %, meaning that we can dismiss other inputs, such as nearby paleorivers, as a major component of material at this site (Drake et al., 2010; Skonieczny et al., 2015). From 26 ka to the end of the LGM, dust fluxes show a slight decrease punctuated by abrupt rises and falls between values of ~4.5 to ~2 g cm^{-2} kyr^{-1}, including a small peak coincident with H2 (24 ka) and a prominent peak at ~21 ka. Dust fluxes then rise to peaks during H1 (~6 g cm^{-2} kyr^{-1}) and the YD (~4.2 g cm^{-2} kyr^{-1}), before decreasing to a minimum during the AHP (0.39-0.49 g cm^{-2} kyr^{-1}). In contrast to cores GC37 and GC49, the H1 peak dust flux is larger than the YD peak dust flux (by ~50%), showing a stronger dust response during H1 at this southern core site. Dust fluxes then increase into the Late Holocene (~2 ka) to a value of 1.64 g cm^{-2} kyr^{-1}.

Opal fluxes are highly correlated with dust fluxes in core GC68 ($r^2 = 0.44$; p-value < 0.05), while organic carbon fluxes show very low correlation ($r^2 = 0.02$; p-value > 0.05). From 26 ka, the end of the core, to the end of the LGM opal fluxes show a slight decrease punctuated

by abrupt rises and falls similar to the dust record, also recording peaks coincident with H2 and at ~21 ka. Organic carbon fluxes show a substantial difference from dust fluxes from 26 ka to the end of the LGM with no noticeable trend and high variability. Biogenic fluxes rise to high levels during both H1 and the YD, with the YD peak slightly larger than the H1 peak in both opal and organic carbon fluxes. Fluxes of both opal and organic carbon fall to low levels throughout the AHP before rising during the late Holocene.

3.4 ODP 658C (21°N)

The ODP 658C core provides a longer archive than the CHEETA cores and allows continued high-resolution study of dust accumulation rates to the margin. Here we extend the record back to 67 ka. The early portion of the record at the latter stages of MIS 4 shows moderate dust fluxes to the margin followed by an abrupt peak (2.4 g cm^{-2} kyr^{-1}) coincident with H6 (62.5 ka). This is followed by a decline in dust flux over 3 ka to an interval from 60-50 ka when the lowest dust fluxes (0.18 g cm^{-2} kyr^{-1}) observed in the record for this site are recorded. This low dust interval is interrupted by an abrupt (millennial-scale) dust increase to the highest fluxes (2.5 g cm^{-2} kyr^{-1}) observed in the whole record centered at H5a (55 ka). A trend of increasing dustiness is then observed after the end of the 60-50 ka low dust interval, reaching a maximum (~2.1 g cm^{-2} kyr^{-1}) at 35 to 33 ka. Millennial-scale variability is superimposed on this broad trend, including a peak in flux (1.8 g cm^{-2} kyr^{-1}) coincident with H5 (48 ka). Dust fluxes decrease from the late MIS 3 maximum to ~1 g cm^{-2} kyr^{-1} at the end of the LGM (20 ka), with millennial-scale abrupt peaks in flux of 2 g cm^{-2} kyr^{-1} and 2.26 g cm^{-2} kyr^{-1}, coincident with H3 (31.3 ka) and H2 (24 ka) respectively. Following the LGM, the remainder of the dust record from this site is a detrital flux record (Adkins et al., 2006), as grain size-based estimates of the aeolian fraction of detrital sediments are not available. Detrital fluxes rise to millennial-scale peaks during Hl (1.94 g cm^{-2} kyr^{-1}) and the YD (2.12 g cm^{-2} kyr^{-1}) before decreasing to sustained low values (0.75-1 g cm^{-2} kyr^{-1}) during the AHP; a hiatus occurs during H1, so the peak of H1 fluxes is missing in this record. Detrital fluxes increase abruptly at 5 ka and continue to rise steadily into the Late Holocene to a value of ~2 g cm^{-2} kyr^{-1}.

Both opal and organic carbon fluxes are positively correlated with dust fluxes in core ODP 658C ($r^2 = 0.46$; p-value < 0.05 and $r^2 = 0.32$; p-value < 0.05, respectively). Both opal and organic carbon fluxes increase from moderate values at the end of MIS 4 to two peaks coincident

with H6 and H5a separated by an interval of lower fluxes, with the organic carbon showing higher amplitude rises and falls during the interval of lower fluxes. Biogenic fluxes variably rise and fall from H5a until ~45 ka when both opal and organic carbon fluxes gradually increase to a maximum at 38 to 34 ka. Both opal and organic carbon fluxes drop sharply at 33 ka and remain low throughout MIS 2 and the LGM, with small peaks at H3 and H2. The opal flux record shows peaks during H1 and the YD, falls to low levels throughout the AHP, and rises during the late Holocene. From the end of the LGM to the Holocene organic carbon concentrations have not been measured.

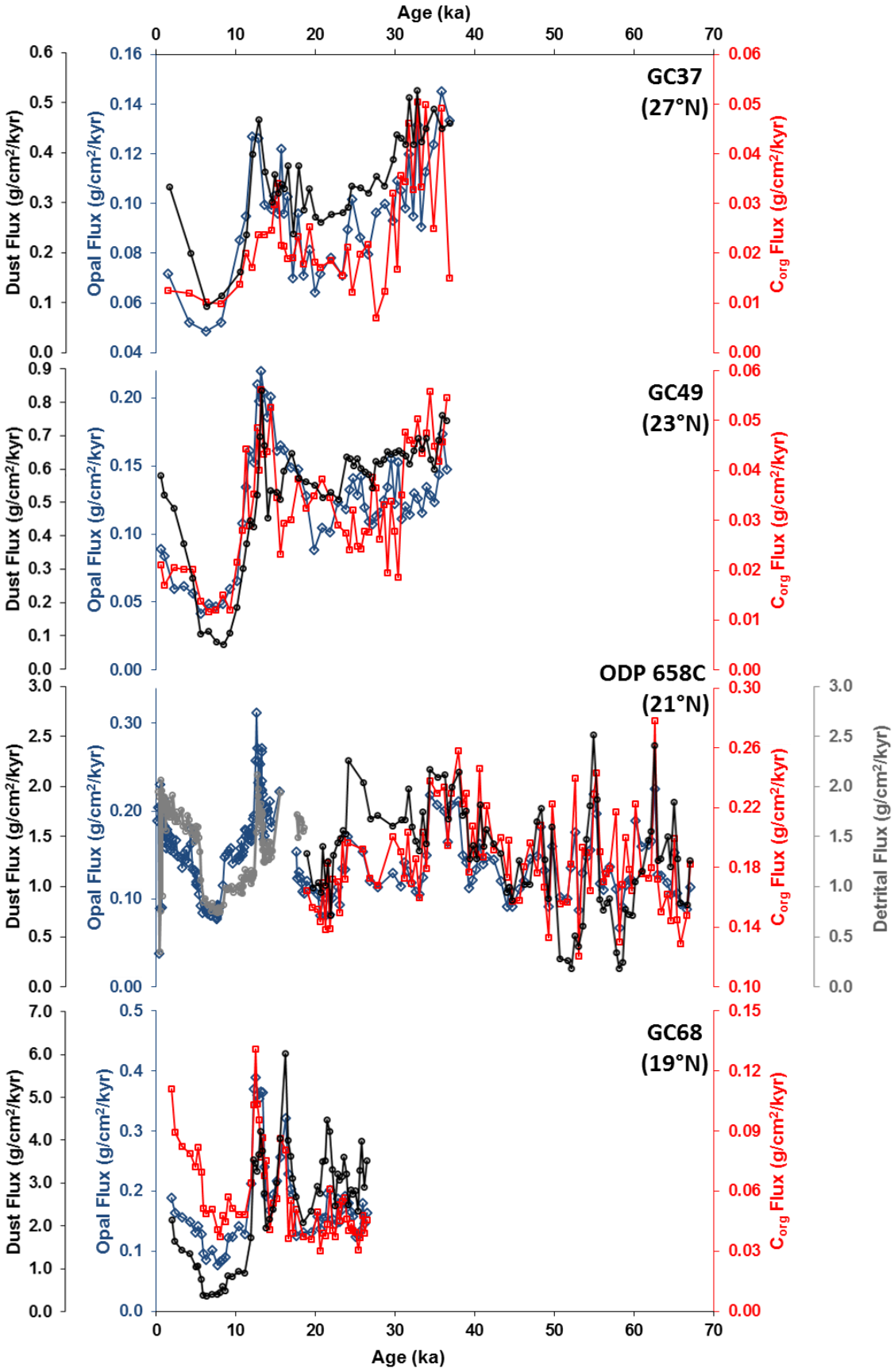
Age (ka)
GC37
(27°N)
GC49
(23°N)
ODP 658C
(21°N)
GC68
(19°N)
Dust Flux (g/cm²/kyr)
Opal Flux (g/cm²/kyr)
Corg Flux (g/cm²/kyr)
Detrital Flux (g/cm²/kyr)

389

Figure 2. Opal (blue line, open diamonds), C_{org} (red line, open squares), dust (black line, open circles), and detrital (grey line, open circles) flux records arranged from north to south as labeled. Data <20 ka in GC37, GC49, and GC68 from Bradtmiller et al., (2016); data <20 ka in ODP 658C from Adkins et al., (2006).

4 Discussion

4.1 Coherence of African Margin and Mid-Atlantic Dust Flux Records

This work has extended the CHEETA dust flux records to the bottom of cored material reaching back to 37 ka in GC37, 36.5 ka in GC49, and 26.5 ka in GC68, and produced a dust flux record from 67 to 19 ka for the core from ODP Hole 658C (Figure 3). The extended portions of the ODP 658C, GC37, and GC49 records overlap from 37 ka to 20 ka and demonstrate coherent variation on both orbital and millennial timescales. In ODP 658C, Heinrich events 2 and 3 are recorded as increases in dust flux superimposed on a decreasing trend of dustiness through the end of the LGM. The GC68 record also shows H2 recorded as a time of increased dust flux, and a decreasing trend of dustiness through the end of the LGM, while also showing higher frequency variability from 26 to 20 ka with multiple abrupt peaks in dust flux. In the northern core sites (ODP 658C through GC37, 21°-27°N), peak dust fluxes in early MIS 2 (27 to 23 ka) are similar to modern, and only in the southernmost core site (GC68, 19°N) are early MIS 2 fluxes higher than modern (by ~50%). In all cores, dust fluxes drop from early MIS 2 to the LGM (23 to 19 ka) by 20-40%. The strong agreement between dust records from 37 to 19 ka gives us confidence that the extended ODP 658C record from 67 to 37 ka is faithfully recording the export of dust to the margin.

The ODP 658C record shows remarkable similarity to the dust flux record covering the last 70 ka from the Mid-Atlantic at 25°N (Middleton et al., 2018), both in overall trends and millennial-scale variability (Figure 4). Both records exhibit a background increase in dustiness throughout MIS 3, a large decrease during the AHP, and peaks in dust flux during Greenland stadials. There are two distinct times of disagreement between the records, namely during the AHP through the late Holocene, and from 60 to 50 ka. In the Mid-Atlantic record, the AHP has a more gradual onset and ends 2 ka later than in the ODP 658C record. From 60 to 50 ka the ODP 658C record exhibits much higher variability with fluxes reaching both their maximum and minimum levels of the whole 67 ka record. These disagreements are likely a consequence of low

sedimentation rates at the Mid-Atlantic site (averaging 2 cm/kyr), whereas the ODP 658C site has an average sedimentation rate of 16 cm/kyr. The high amplitude and abrupt changes in dust flux during the AHP and the 60 to 50 ka humid period are well resolved due to the high sedimentation rates at the ODP 658C site (Figure 4), whereas the amplitude of these abrupt changes may have been smoothed due to the much lower sedimentation rate and thus greater influence of mixing by bioturbation at the Mid-Atlantic site.

The agreement with the Mid-Atlantic dust record, which lies thousands of miles downwind of African dust sources, is important in that the site is likely to be biased toward summer rather than winter dust emissions, and it presumably reflects dust from a wider region of North Africa than the margin sites. Consistent with previous work (Williams et al., 2016), this comparison suggests that the summer and winter dust plumes, and dust deposition at both proximal and distal sites, have largely varied in sync over the late Pleistocene. The agreement also builds confidence that the variations in sea-level (and thus in the distance to dust source areas) has not had a substantial influence on dust deposition at the margin sites. Therefore, the ODP 658C dust record appears to be representative of an integrated signal of African dust export to the North Atlantic over the past 67 ka.

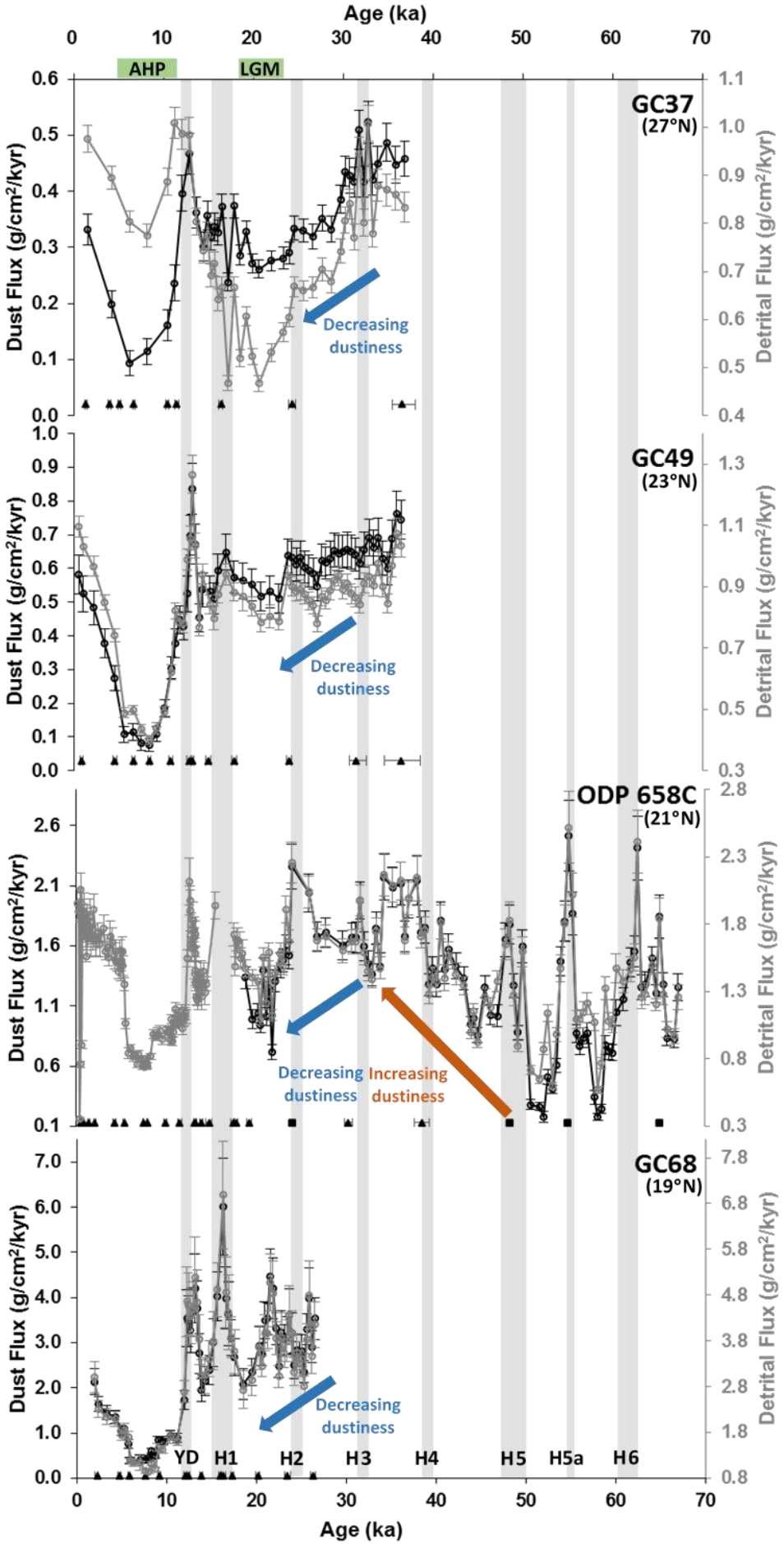
Age (ka)
AHP
LGM
GC37
(27°N)
Dust Flux (g/cm²/kyr)
Detrital Flux (g/cm²/kyr)
Decreasing dustiness
GC49
(23°N)
ODP 658C
(21°N)
Decreasing dustiness
Increasing dustiness
GC68
(19°N)
YD
H1
H2
H3
H4
H5
H5a
H6

Figure 3. Dust (black line, open circles) and detrital (grey line, open circles) flux records arranged from north to south as labeled with 1σ uncertainties shown. Data <20 ka in GC37, GC49, and GC68 from McGee et al., (2013), data <20 ka in ODP 658C from Adkins et al., (2006). ^{14}C tie points and 1σ uncertainties shown as black triangles, $CaCO_3$ tie points for ODP

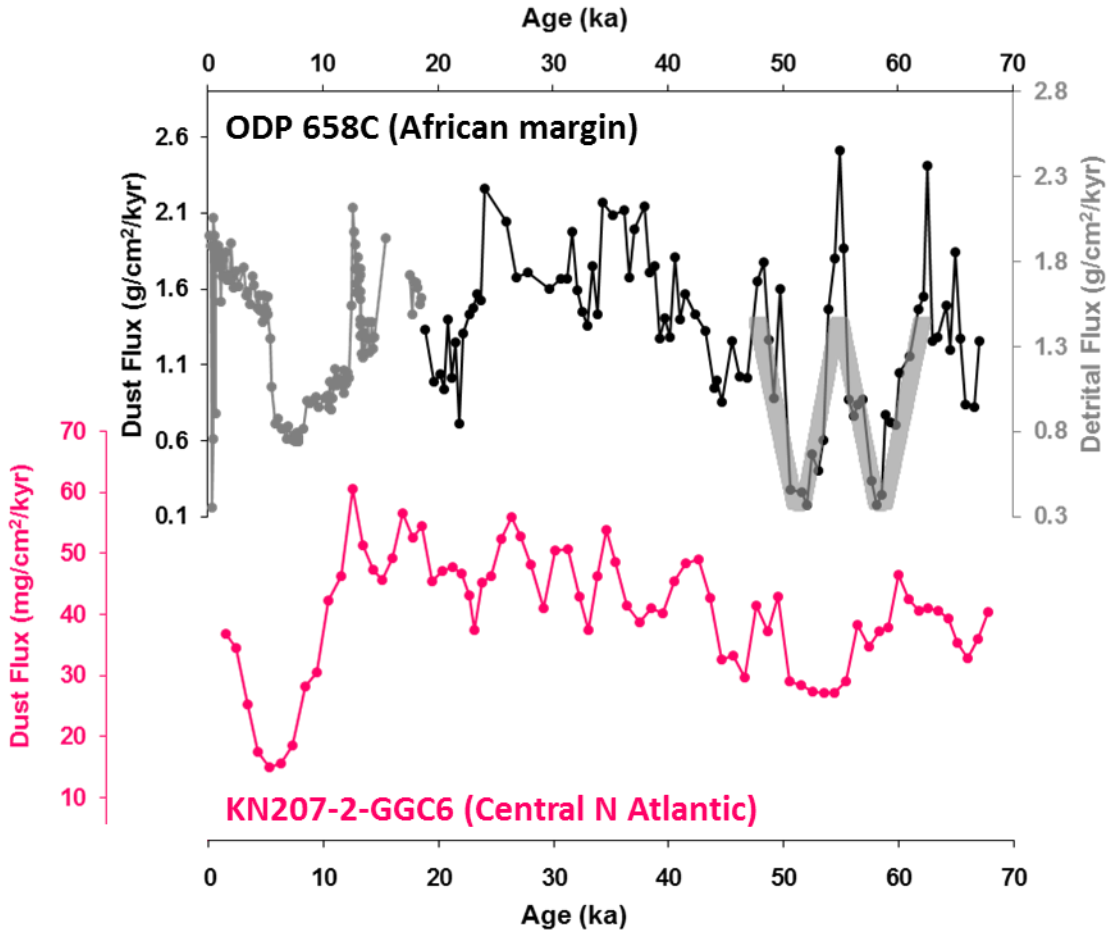

658C shown as black squares.

Figure 4. ODP 658C dust and detrital flux records (black and grey lines, respectively) and KN207-2-GGC6 dust flux record from the mid-Atlantic (Middleton et al., 2018) (pink line). Data <20 ka in ODP 658C from Adkins et al., (2006). "W-shape" structure of the dust flux record as referred to in main text is illustrated by a transparent grey w-shape from ~60 to 50 ka.

4.2 Major Features of Dust Flux Records from 67 to 20 ka (MIS 4 through 2)

We begin by describing the broader-scale features of the records before turning to millennial-scale variability. At the onset of MIS 3 (~60 ka) Northern Hemisphere temperatures

increase, and during this time dust fluxes in ODP 658C drop to values comparable to those during the AHP (a direct comparison of dust fluxes is not possible because Adkins et al. (2006) reported total detrital fluxes, providing only an upper bound on dust fluxes). Over the next 30 ka, Northern Hemisphere high-latitude temperatures reflected in Greenland ice core records decrease gradually to minimum values between 30 and 25 ka, with multiple millennial-scale stadials superimposed on the background decrease (Figure 5; colder temperatures are oriented upwards) (Seierstad et al., 2014). Dust fluxes over this interval show a gradual increase to sustained high values during the end of MIS 3 and early MIS 2, with millennial-scale pulses of high dust flux superimposed on the background increase.

During MIS 2, Northern Hemisphere high-latitude temperatures gradually increase after 24 ka leading into the LGM time slice commonly targeted for data-model comparisons (23 to 19 ka) (e.g., Waelbroeck et al., 2009). Dust fluxes over this interval decrease from the high values observed at 30 to 25 ka; as a result, in all but the southernmost core (GC68, 19°N) the LGM is characterized by dust deposition rates that are similar to late Holocene fluxes. The broad scale features of the dust records from the end of MIS 4 through the end of MIS 2 show a strong correspondence over this interval between high latitude temperatures and dust fluxes to the margin, with lower temperatures associated with higher fluxes to the margin and higher temperatures associated with lower fluxes to the margin.

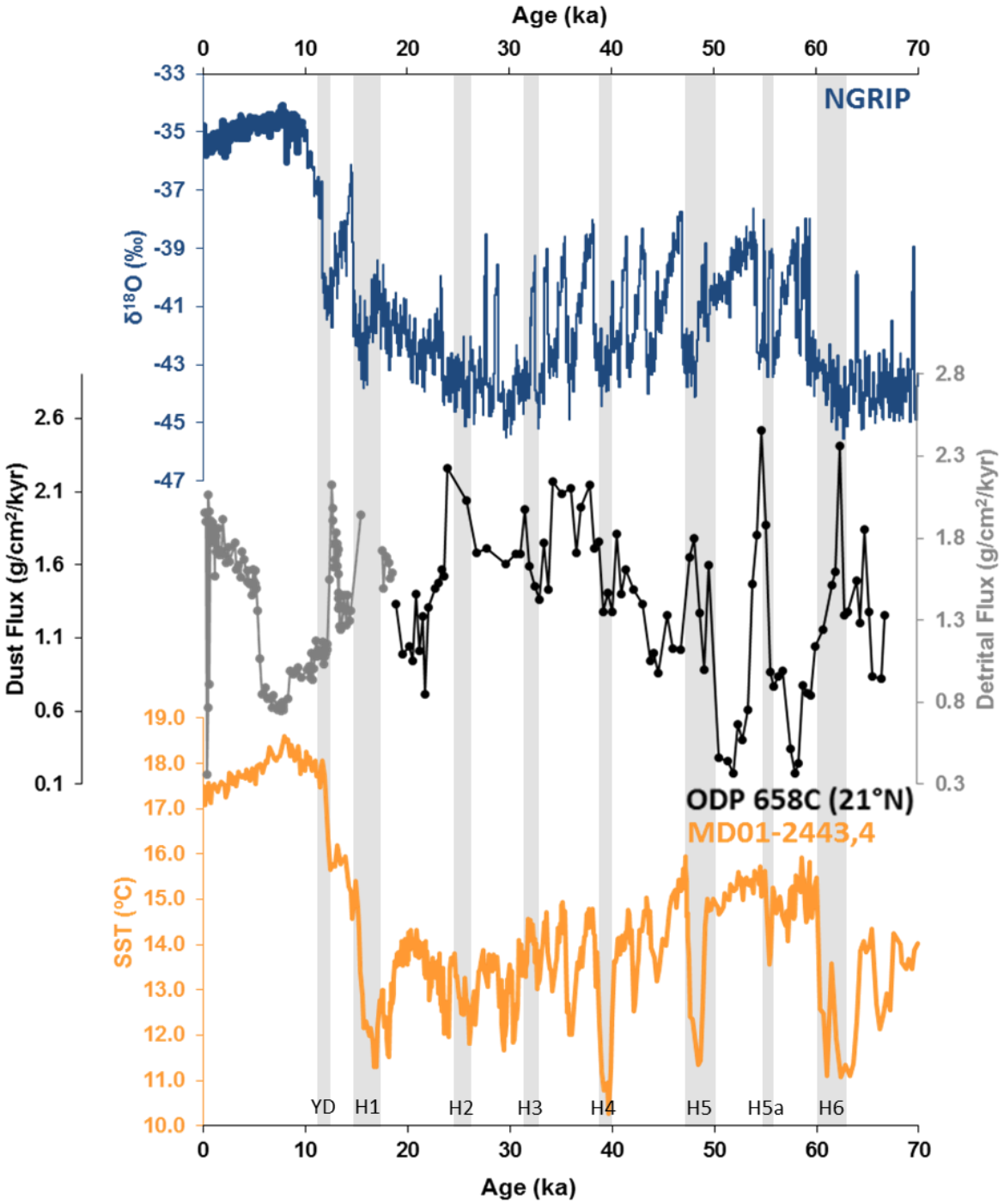

Figure 5. NGRIP $\delta^{18}O$ from Seierstad et al., (2014) (blue line), ODP 658C dust and detrital flux records (black and grey lines, respectively), and MD01-2443,4 SST record from Martrat et al., (2007) (orange line). Data <20 ka in ODP 658C from Adkins et al., (2006).

The high sedimentation rates and well-resolved radiocarbon-based age model for GC68 allows a more detailed comparison between dust flux variability and millennial-scale high latitude climate records over the last 26 ka. The millennial-scale features in the GC68 dust flux record associated with high-latitude climate fluctuations during H1, the Bølling-Allerød warm period, and the YD, previously described by McGee et al., (2013), show strong coherence between North Atlantic stadials and high fluxes of dust to the West African margin. Comparison of the earlier highly-resolved 26.5 to 20 ka portion of the GC68 flux record (Figure 6) with a proxy record of North Atlantic SSTs (Cacho et al., 1999) reveals that the three cold events at 25 ka, 24 ka (H2) and 21 ka are all associated with increases of dust flux to the margin. The amplitudes of dust flux over this interval do not have a clear correspondence with amplitude of SST (i.e. the largest dust flux peak does not occur at the time of coldest SST), which could be caused by variable bioturbation and smoothing of the peaks in the two records.

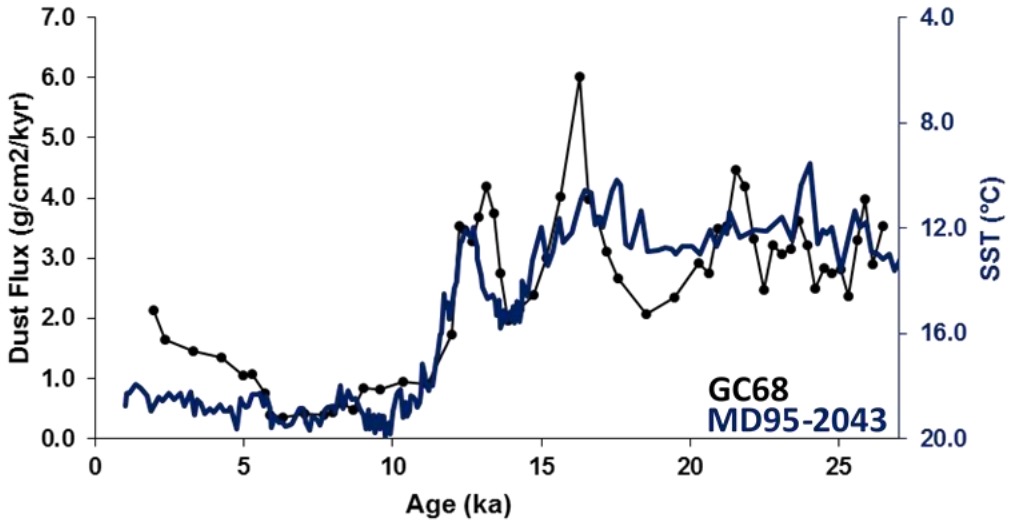

Figure 6. GC68 dust flux record (black line) and MD95-2043 SST record from Cacho et al., (1999) (blue line). Data <20 ka in GC68 from McGee et al., (2013).

While the GC68 cored material ends at 26.5 ka, the older material from CHEETA cores GC37 and GC49 and ODP Core 658C shows peaks of dust flux likely associated with earlier millennial-scale North Atlantic stadial events. At 62.5 ka there is a pronounced stadial (including Heinrich event 6) in the North Atlantic with an accompanying millennial-scale peak in which

dust fluxes at ODP 658C more than double. This signal of increased dust during stadials with associated Heinrich events is a robust response, with dust increases seen at H5a, H5, H3, and H2. The exception to this is H4 which occurs at a time in ODP 658C where dust is at a minimum; we suggest that this mismatch is due to age model error (see Supplementary Information S1), and that the subsequent dust flux peak is a response to H4. A similar mismatch is evident in the mid-Atlantic record of Middleton et al. (2018). There are also stadial events (without accompanying H events) with pronounced dust flux peaks at 42 ka and 37 ka, showing that increased export of dust is observed during stadials both with and without H events. There are multiple instances in which stadials are observed in the SST record without discernible increases in dust flux (67 ka, 47 ka, 30 ka), perhaps due to aforementioned age model error, or increased smoothing by bioturbation during times of lower sedimentation rates (see Supplementary Information S2).

Based upon the strong coherence between millennial-scale peaks in dust flux in our most robust record (GC68) with stadials in the North Atlantic, we suggest that the millennial-scale peaks in the longer dust flux records (ODP 658C, GC49, GC37) correspond to the millennial-scale stadial events in the North Atlantic SST records, and that any mismatches are likely due to issues with smoothing and age control. This conclusion, which could be strengthened by additional records with consistently high accumulation rates as in CHEETA core GC68, suggests that the impact of Heinrich events on West African climate was largely stable across varying orbital configurations and ice sheet extents during MIS 2, 3, and 4.

4.3 Implications for Wind and Precipitation Changes over North Africa During North Atlantic Cooling Events

These new data, in combination with previously published records, provide a clear picture of climate changes in stadial times in North Africa. First, it is clear that stadials are marked by both precipitation decreases and strengthening of northeasterly winds over North Africa. Stadials are marked by reduced precipitation in the Sahel and a southward shift of the Sahel/Sahara boundary (Collins et al., 2013; Weldeab et al., 2007). In the Sahara, leaf wax δD data from the CHEETA cores spanning the last 25 ka also document dry conditions in northwest Africa during stadial events (Tierney et al., 2017). However, northwest African margin δD values are no more positive during stadials than in the late Holocene (Figure 7), perhaps because precipitation cannot decrease much more than its current levels in the Sahara.

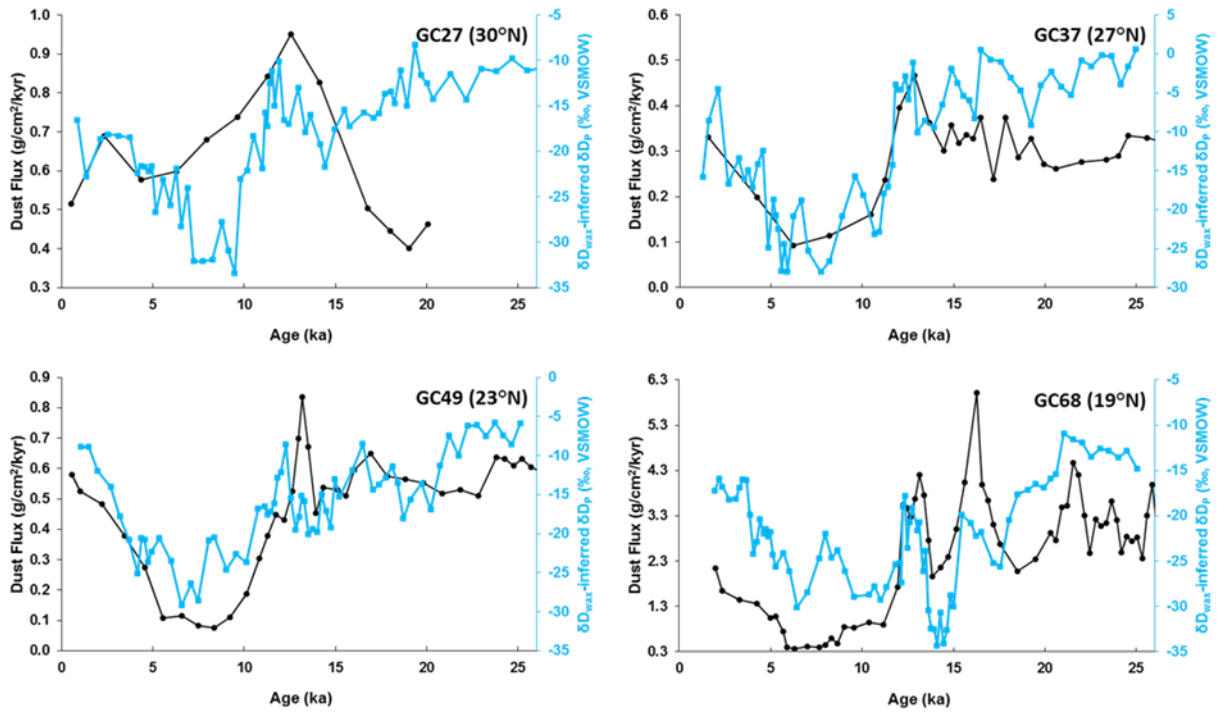

Figure 7. Dust flux records (black line) and δD_{wax}-inferred hydrogen isotopic composition of precipitation records (δD_P) (blue line; Tierney et al., 2017) at CHEETA sites GC27, GC37, GC49, and GC68 as labeled (black lines). Data <20 ka in GC27, GC37, GC49, and GC68 from McGee et al., (2013).

For the Saharan dust sources relevant for the northwest African margin and central Atlantic cores, increased aridity is thus unlikely to explain dust fluxes roughly double late Holocene values during stadials. Instead, Murphy et al. (2014) suggest that in areas that are already dry and dust producing like the Sahara, the only way to increase dust export is through an increase in wind speed; this conclusion is supported by studies supporting the dominant role of winds in modern decadal variability in Saharan dust emissions (Ridley et al., 2014; Wang et al., 2015). Consistent with this conclusion, our records show strong covariation of opal and organic carbon fluxes with dust fluxes throughout most of our records (Figure 7), providing firm evidence for intensification of northeasterly winds as a driver of increases in both coastal upwelling and dust deposition during stadials (Bradtmiller et al., 2016; McGee et al., 2018).

Another potential mechanism which could explain the covariation is ballasting of organic material by dust particles. This has been shown to occur off Mauritania with Saharan dust ballasting organic matter (van der Jagt et al., 2018), potentially increasing export by an order of magnitude, however this mechanism is unlikely to explain the covariation of opal fluxes with dust export.

A modeling study by Liu et al. (2014) highlights the importance of these wind anomalies in communicating stadial conditions to the West African monsoon, demonstrating that anomalous northeasterly winds resulting from high-latitude cooling advect cold, dry air into North Africa, weakening the west African monsoonal circulation and drying the Sahel. This cold air advection is amplified by water vapor feedbacks, which further cool the Sahara and raise surface pressures, increasing northeasterly winds even more (Liu et al., 2014). Our dust and biogenic flux records thus provide support for Liu et al.'s ventilation mechanism as a driver of the reductions in Sahel rainfall suggested by proxy data during stadials (e.g., Weldeab et al., 2007). In stadials, as in modern decadal-scale variability (Wang et al., 2015), reduced Sahel precipitation occurs in association with strengthened northeasterly winds over the Sahara.

Combining West African margin dust flux and dust percentage data to form a north-south transect (Figure 8a), we also observe important latitudinal differences in the wind anomalies associated with different stadial events. These differences are most robust during H1 and the YD, periods for which dating uncertainties are relatively small and the most records exist. In records south of 20°N, dust increases during H1 are especially prominent, while dust changes during the YD relatively muted. The opposite is true north of 20°N, as the YD dust flux peak is substantially greater than the H1 peak at 23°N and 27°N. Figure 8b shows a consistent increase in the YD:H1 dust flux ratio with increasing latitude.

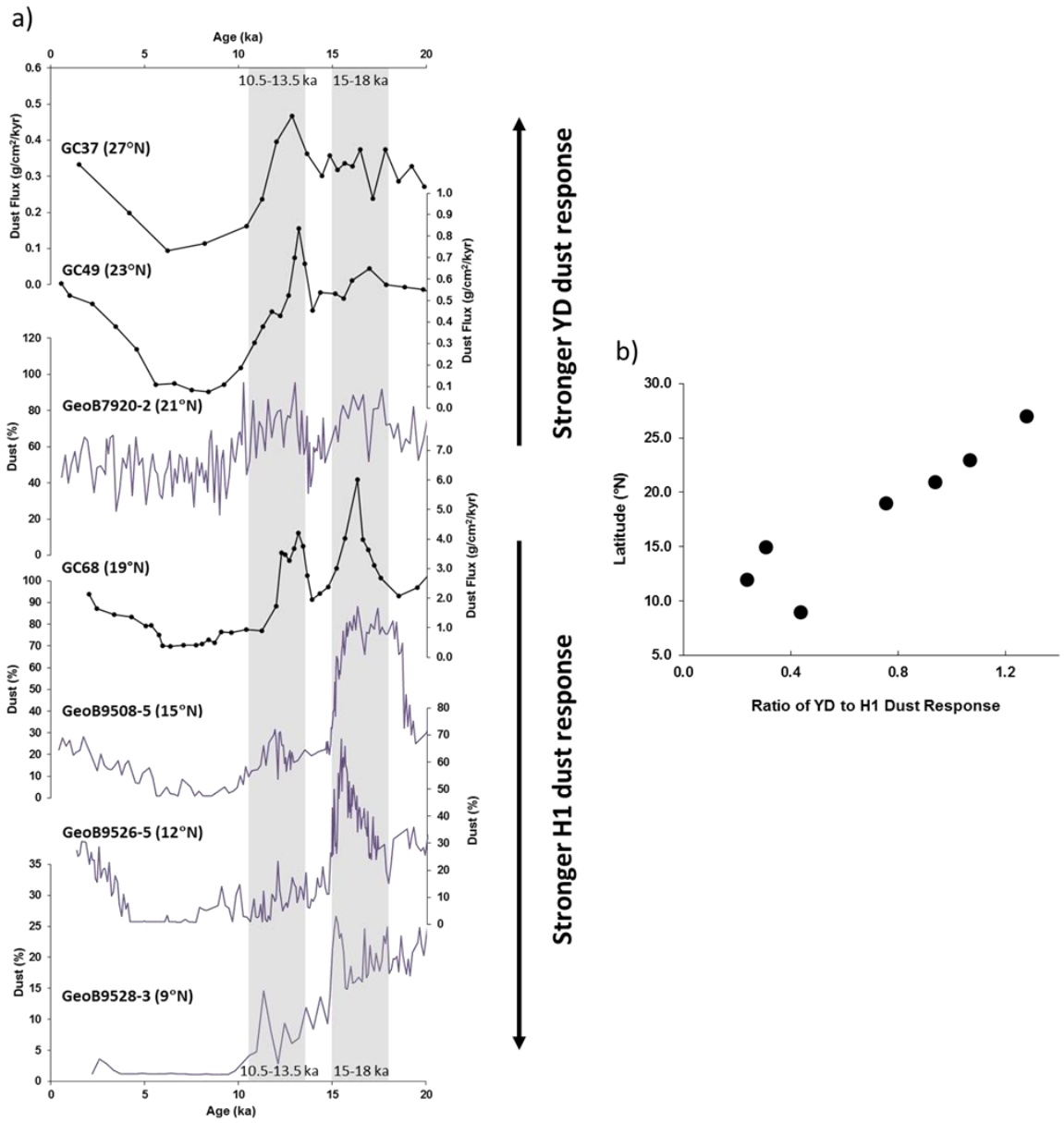

Figure 8. a) North-south transect along the West African margin of dust flux records (black line; McGee et al., 2013) and dust percentage records (purple line; Collins et al., 2013) b) Ratio of Younger Dryas to Heinrich event 1 dust response versus latitude. All records were interpolated to a resolution of 0.1 kyr, and a ratio of YD to H1 dust response was calculated using the maximum value of the 0.5 kyr running means from within the time interval from 10.5-13.5 ka (the Younger Dryas) and the time interval from 15-18 ka (Heinrich event 1). These broad intervals were chosen in order to encompass age model uncertainty between the records.

574 This observation suggests that northeasterly wind anomalies over North Africa peaked
575 south of 20°N in H1, and north of 20°N in the YD. This different atmospheric response may
576 reflect changing boundary conditions, and in particular smaller ice sheets in North America and
577 Europe, between H1 and the YD; alternatively, it may reflect differences in sea ice responses in
578 the two events. This difference in wind response in turn implies differences in the wind-driven
579 ocean circulation in the subtropical North Atlantic during the YD and H1.
580
581 4.4 Relationship Between Summer Insolation and NW African Climate During MIS 4
582 through 2
583 In the new extended ODP 658C dust record extremely low dust fluxes are observed
584 during the insolation maximum centered on 55 ka (Figure 9; low insolation values are oriented
585 upwards). The values seen in terms of detrital flux are even lower than those recorded during the
586 Green Sahara interval at 11 to 5 ka, where diverse proxy evidence indicates much higher rainfall
587 supporting divers vegetation, permanent lakes, and human populations (Gasse, 2000; Jolly et al.,
588 1998; Kuper & Kröpelin, 2006; McGee & deMenocal, 2017; Tierney et al., 2017). Just as in the
589 AHP, opal fluxes are low, suggesting reduced northwesterly wind strength during this wet
590 period. The expression of the 60 to 50 ka low dust event differs from the AHP, however, in that
591 it is punctuated by an abrupt millennial-scale increase in dust at 55 ka associated with H5a. Dust
592 fluxes begin high at 60 ka (1.5 g cm^{-2} kyr^{-1}), decrease by a factor of three at 58 ka (0.5 g cm^{-2}
593 kyr^{-1}), increase dramatically at 55 ka (2.5 g cm^{-2} kyr^{-1}), and decrease to minimum values again at
594 52 ka (0.5 g cm^{-2} kyr^{-1}), before increasing gradually throughout the next 15 ka. This high dust
595 flux event indicates that high-latitude climate can exert a strong influence on African climate
596 even during a time of high summer insolation and a strong West African monsoon.

597

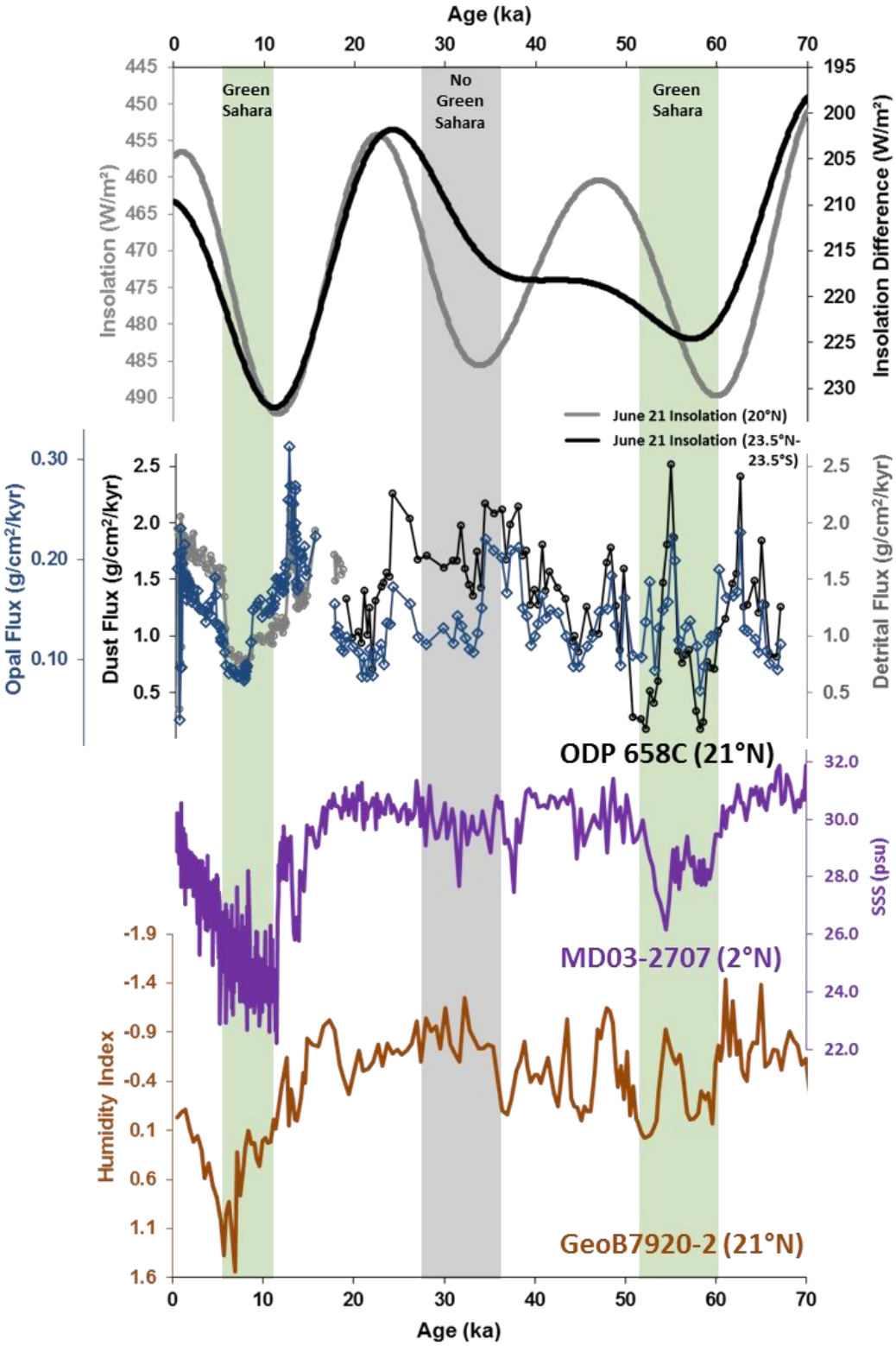
Age (ka)
Green Sahara
No Green Sahara
Green Sahara
Insolation (W/m²)
Insolation Difference (W/m²)
June 21 Insolation (20°N)
June 21 Insolation (23.5°N-23.5°S)
Opal Flux (g/cm²/kyr)
Dust Flux (g/cm²/kyr)
Detrital Flux (g/cm²/kyr)
ODP 658C (21°N)
SSS (psu)
MD03-2707 (2°N)
Humidity Index
GeoB7920-2 (21°N)
Age (ka)

Figure 9. June 21 insolation at 20°N and cross-equatorial insolation gradient (calculated as the difference in June 21 insolation between 23.5°N and 23.5°S) from Laskar et al., (2004) (dark grey solid and dark grey dashed lines, respectively), ODP 658C dust and detrital flux records (black and light grey lines with open circles, respectively), MD03-2707 sea surface salinity (SSS) record, taken to reflect freshwater input from the Sanaga and Niger rivers to the eastern Gulf of Guinea, from Weldeab et al., (2007) (purple line), and GeoB7920-2 Humidity Index record from Tjallingii et al., (2008) (brown line). Data <20 ka in ODP 658C from Adkins et al., (2006).

Comparison of the dust flux record at 60 to 50 ka with other paleoclimate archives of North African climate allows further probing of the structure of the Green Sahara event and how the interplay of high-latitude climate forcing with high summer insolation affects North African hydroclimate. The "W-shape" structure observed in the ODP 658C dust record is also observed in sea surface salinity (SSS) reconstructions in the eastern Gulf of Guinea, taken to reflect freshwater input from the Sanaga and Niger rivers, (Weldeab et al., 2007) and grain size-based continental humidity reconstructions off Cape Blanc (Tjallingii et al., 2008) suggesting a wetter tropical and subtropical North Africa. Wet conditions are also suggested by a low-resolution leaf wax record from ODP 659, which shows quite depleted δD values at ~50 ka (Kuechler et al., 2013).

The "W-shape" structure in the river discharge and humidity records differ somewhat from the dust record, as they show wetter conditions following the 55 ka stadial event, while the dust record shows equal magnitude dust flux minima preceding and following the stadial. Further, the salinity and grain size records both suggest that the 60 to 50 ka wet period was substantially drier than the Holocene AHP, while the detrital flux record of ODP 658C shows values during the 60 to 50 ka time slice comparable to that of the 12 to 5 ka interval. Future work will be required to explore the variable expression of this MIS 3 Green Sahara period in different regions of North Africa using different proxies, and the reason for the extreme expression of the AHP in many proxy records compared to earlier Green Sahara intervals. Potential avenues of exploration include effects of bioturbation, smoothing due to higher frequency climatic events in some intervals, and compaction of material downcore of the AHP leading to a bias in its expression compared to other wet periods.

Dust export to ODP 658C during the local summer insolation maximum from 35 to 28 ka has no discernible minimum in flux, as dust flux remains relatively high throughout this time, unlike the dust minima seen during the previous insolation maximum/Green Sahara interval from 60 to 50 ka, and the following insolation maximum/Green Sahara interval from 12 to 5 ka. The expression of this interval of insolation maximum (35 to 28 ka) in other records of North African hydroclimate is also as a time of aridity, with very high sea surface salinity (interpreted as low freshwater runoff from North Africa) in the Gulf of Guinea (Weldeab et al., 2007) and very low humidity index (interpreted as a high ratio of aeolian to fluvial sediments) in sediments near ODP 658C (Tjallingii et al., 2008). "Skipped beats" of insolation are similarly evident in the last two glacial periods in a dust flux record from the northwest African margin (Skonieczny et al., 2019) and a leaf wax δD records from East Africa (Tierney et al., 2017). In contrast, fluxes of C_{org} and opal decrease by a factor of ~2 over this time interval (Figure 9), but do not reach the minima observed in the Holocene and early MIS 3 Green Sahara intervals. This discrepancy, with dust fluxes staying relatively high throughout the insolation maximum while biogenic proxies decrease, may reflect a decrease in wind strength without a substantial decrease in aridity. Alternatively, the reduced biogenic fluxes may result from changes in the nutrient content of upwelled waters or effects on upwelling and productivity from changing shelf morphology due to sea-level lowering.

The latter part of this arid interval is coincident with the coldest high latitude temperatures during the past 70 ka as measured in Greenland ice, and the coldest North Atlantic SSTs. The precessional beat of maximum local summer insolation at 35 to 28 ka thus occurs during a colder interval with higher ice volume than the preceding and subsequent Green Sahara intervals, suggesting that high latitude forcing during a time of high ice volume and cold temperatures may override the impact of increased summer heating of North Africa on the monsoon, keeping North Africa arid.

Alternatively, the lack of response to high local summer insolation at 35 to 28 ka could be due to the fact that the precessional extreme occurs in association with low obliquity. As a result, high latitude NH summer insolation and the cross-equatorial insolation gradient (calculated as the difference in June 21 insolation between 23.5°N and 23.5°S) remain low despite the maximum in 20°N summer insolation. We note that while much monsoon literature has focused on 65°N summer insolation, recent modeling experiments suggest that the cross-

equatorial insolation gradient (which varies in phase with 65°N insolation) is more directly related to North African monsoon strength (Bosmans et al., 2015; Mantsis et al., 2014).

Modeling by Singarayer et al., (2017) appears to support the first suggestion. In their simulations, the summer rain belt over North Africa reaches similar latitudes during the summer insolation maxima at ~35 ka and ~55 ka when only orbital parameters and greenhouse gases are changed, but the rain belt is substantially farther south at 35 ka when ice sheets are included in the simulation.

5 Conclusions

Extended dust flux records from 19°N to 27°N along the West African margin show a coherent signal of dust export during overlapping intervals, from 37 ka to present in cores GC37, GC49, and ODP 658C, and additionally in core GC68 from 26 ka to present. These records show a peak in dust at 35 to 33 ka, with fluxes decreasing throughout MIS 2; these multi-millennial trends appear to correlate with high-latitude temperature changes indicated by Greenland ice cores, with dust peaking during the coldest conditions. Due to the decline in dust fluxes in MIS 2, the LGM time slice commonly targeted in modeling experiments is marked by relatively moderate dust fluxes. The existence of dust deposition similar to Late Holocene levels in most cores despite the presence of large ice sheets and much steeper pole-to-equator surface temperature gradients is worthy of further investigation.

There is also coherent millennial-scale variability throughout our records. In core GC68, which has the highest accumulation rates and best-constrained age model in MIS 2, millennial-scale dust peaks correspond with reductions in North Atlantic SSTs. At other sites, most stadial events—including H2, H3, H5, H5a, and H6—correspond to periods of high dust fluxes. Due to this strong coherence, we suggest that the few intervals in which high dust fluxes are not observed at the same time as low SSTs result from age model errors and/or bioturbation. Covariation of dust fluxes with fluxes of opal and organic carbon, taken here to represent coastal upwelling intensity, suggests that dust flux peaks during stadials and are likely driven by increases in northeasterly wind strength. This finding provides support for the role of northeasterly winds in ventilating the West African monsoon during stadial events, leading to the observed decreases in Sahel precipitation. Examining a broad suite of dust records along the northwest African margin, we also find differences in wind anomalies associated with different

stadials, with wind anomalies peaking south of 20°N during H1 and north of 20°N during the YD, perhaps due to changing ice sheet topography.

The longer dust flux record from ODP 658C reveals a "Green Sahara" interval at 60 to 50 ka marked by low dust fluxes. This period corresponds to a time of high NH summer insolation and relatively warm North Atlantic SSTs, suggesting a strong West African monsoon even in the presence of extended ice sheets and moderate atmospheric CO_2 concentrations. This interval differs from the AHP (12 to 5 ka), as there is a millennial-scale peak in dust flux during the interval that appears to correspond to H5a. The low latitude summer insolation maximum at 35 ka is a "skipped beat", in that there is no record of a strengthening of the west African monsoon and decrease in dust flux during this time, potentially due either to a reduced cross-equatorial insolation gradient during this time of low obliquity, or to the influence of cold North Atlantic temperatures and large ice sheets in counteracting the local insolation forcing on North African climate.

Acknowledgments, Samples, and Data

The data supporting the conclusions is included in the Supporting Information as a separate dataset for each core site for review purposes. This data is in the process of being archived and will be submitted to the NOAA/WDS for Paleoclimatology archives by time of publication with an in-text citation. We would like to thank I. Tal and E. Steponaitis at MIT for laboratory assistance. We would also like to thank the crew, staff and scientists of R/V Oceanus cruise 437-7, and co-chief scientists Tim Eglinton and Thomas Wagner. This research used samples provided by the Ocean Drilling Program (ODP). This research was supported by NSF #OCE-1103262 to L. Bradtmiller, NSF #OCE-1030784 to D. McGee, P. deMenocal and G. Winckler, and by internal grants from Macalester College and MIT.

References

Adkins, J., deMenocal, P., & Eshel, G. (2006). The "African humid period" and the record of marine upwelling from excess 230Th in Ocean Drilling Program Hole 658C. *Paleoceanography, 21*(4), 1–14. https://doi.org/10.1029/2005PA001200

Andersen, M. B., Stirling, C. H., Zimmermann, B., & Halliday, A. N. (2010). Precise determination of the open ocean $^{234}U/^{238}U$ composition. *Geochemistry, Geophysics,*

Geosystems, *11*(12). https://doi.org/10.1029/2010GC003318

Bacon, M. P. (1984). Glacial to interglacial changes in carbonate and clay sedimentation in the Atlantic Ocean estimated from 230Th measurements. *Chemical Geology*, *46*(2), 97–111. https://doi.org/10.1016/0009-2541(84)90183-9

Battisti, D. S., Ding, Q., & Roe, G. H. (2014). Coherent pan-Asian climatic and isotopic response to orbital forcing of tropical insolation. *Journal of Geophysical Research*, *119*(21), 11,997-12,020. https://doi.org/10.1002/2014JD021960

Bory, A. J.-M., & Newton, P. P. (2000). Transport of airborne lithogenic material down through the water column in two contrasting regions of the eastern subtropical North Atlantic Ocean. *Global Biogeochemical Cycles*, *14*(1), 297–315.

Bosmans, J. H. C., Drijfhout, S. S., Tuenter, E., Hilgen, F. J., & Lourens, L. J. (2015). Response of the North African summer monsoon to precession and obliquity forcings in the EC-Earth GCM. *Climate Dynamics*, *44*(1–2), 279–297. https://doi.org/10.1007/s00382-014-2260-z

Braconnot, P., Harrison, S. P., Kageyama, M., Bartlein, P. J., Masson-Delmotte, V., Abe-Ouchi, A., … Zhao, Y. (2012). Evaluation of climate models using palaeoclimatic data. *Nature Climate Change*, *2*(6), 417–424. https://doi.org/10.1038/nclimate1456

Bradtmiller, L. I., McGee, D., Awalt, M., Evers, J., Yerxa, H., Kinsley, C. W., & deMenocal, P. B. (2016). Changes in biological productivity along the northwest African margin over the past 20,000 years. *Paleoceanography*, *31*(1), 185–202. https://doi.org/10.1002/2015PA002862

Bronk Ramsey, C. (2008). Deposition models for chronological records. *Quaternary Science Reviews*, *27*(1–2), 42–60. https://doi.org/10.1016/j.quascirev.2007.01.019

Cacho, I., Grimalt, J. O., Pelejero, C., Canals, M., Sierro, F. J., Flores, J. A., & Shackleton, N. (1999). Dansgaard-Oeschger and Heinrich event imprints in Alboran Sea paleotemperatures. *Paleoceanography*, *14*(6), 698–705. https://doi.org/10.1029/1999PA900044

Carlson, T. N., & Prospero, J. M. (1972). The Large-Scale Movement of Saharan Air Outbreaks over the Northern Equatorial Atlantic. *Journal of Applied Meteorology*, *11*, 283–297.

Chiapello, I., Bergametti, G., Gomes, L., Chatenet, B., Dulac, F., Pimenta, J., & Suares, E. S. (1995). An additional low layer transport of Sahelian and Saharan dust over the north-eastern Tropical Atlantic. *Geophysical Research Letters*, *22*(23), 3191–3194.

753 https://doi.org/10.1029/95GL03313
754 Collins, J. A., Govin, A., Mulitza, S., Heslop, D., Zabel, M., Hartmann, J., … Wefer, G. (2013).
755 Abrupt shifts of the Sahara-Sahel boundary during Heinrich stadials. *Climate of the Past*,
756 *9*(3), 1181–1191. https://doi.org/10.5194/cp-9-1181-2013
757 Copernicus Climate Change Service (C3S). (2017). ERA5: Fifth generation of ECMWF
758 atmospheric reanalyses of the global climate. Copernicus Climate Change Service Climate
759 Data Store (CDS). Retrieved May 22, 2020, from
760 https://cds.climate.copernicus.eu/cdsapp#!/home
761 deMenocal, P.B. (1995). Plio-Pleistocene African climate. *Science*, *270*(5233), 53–59.
762 deMenocal, Peter B., Ortiz, J., Guilderson, T., Adkins, J., Sarnthein, M., Baker, L., &
763 Yarusinsky, M. (2000). Abrupt onset and termination of the African Humid Period: Rapid
764 climate responses to gradual insolation forcing. *Quaternary Science Reviews*, *19*(1–5), 347–
765 361. https://doi.org/10.1016/S0277-3791(99)00081-5
766 deMenocal, Peter B., Ortiz, J., Guilderson, T., & Sarnthein, M. (2000). Coherent high- and low-
767 latitude climate variability during the holocene warm period. *Science*, *288*(5474), 2198–
768 2202. https://doi.org/10.1126/science.288.5474.2198
769 deMenocal, Peter B., Ruddiman, W. F., & Pokras, E. M. (1993). Influences of High- and Low-
770 Latitude Processes on African Terrestrial Climate: Pleistocene Eolian Records from
771 Equatorial Atlantic Ocean Drilling Program Site 663. *Paleoceanography*, *8*(2), 209–242.
772 https://doi.org/10.1029/93PA02688
773 Doherty, O. M., Riemer, N., & Hameed, S. (2012). Control of Saharan mineral dust transport to
774 Barbados in winter by the Intertropical Convergence Zone over West Africa. *Journal of*
775 *Geophysical Research Atmospheres*, *117*(19), 1–13. https://doi.org/10.1029/2012JD017767
776 Drake, N. A., Blench, R. M., Armitage, S. J., Bristow, C. S., & White, K. H. (2010). Ancient
777 watercourses and biogeography of the Sahara explain the peopling of the desert.
778 *Proceedings of the National Academy of Sciences*, 1–5.
779 https://doi.org/10.1073/pnas.1012231108
780 Friese, C. A., van Hateren, J. A. Van, Vogt, C., Fischer, G., & Stuut, J.-B. W. (2017). Seasonal
781 provenance changes in present-day Saharan dust collected in and off Mauritania.
782 *Atmospheric Chemistry and Physics*, *17*, 10163–10193. https://doi.org/10.5194/acp-17-
783 10163-2017

Gasse, F. (2000). Hydrological changes in the African tropics since the Last Glacial Maximum. *Quaternary Science Reviews*, *19*(1–5), 189–211. https://doi.org/10.1016/S0277-3791(99)00061-X

Gómez-Letona, M., Ramos, A. G., Coca, J., & Arístegui, J. (2017). Trends in Primary Production in the Canary Current Upwelling System — A Regional Perspective Comparing Remote Sensing Models. *Frontiers in Marine Science*, *4*(November), 1–18. https://doi.org/10.3389/fmars.2017.00370

Hayes, C. T., Anderson, R. F., Fleisher, M. Q., Huang, K., Robinson, L. F., Lu, Y., … Moran, S. B. (2015). Deep-Sea Research II Th and 231 Pa on GEOTRACES GA03 , the U . S . GEOTRACES North Atlantic transect , and implications for modern and paleoceanographic chemical fl uxes. *Deep-Sea Research Part II*, *116*, 29–41. https://doi.org/10.1016/j.dsr2.2014.07.007

Holz, C., Stuut, J. B. W., & Henrich, R. (2004). Terrigenous sedimentation processes along the continental margin off NW Africa: Implications from grain-size analysis of seabed sediments. *Sedimentology*, *51*(5), 1145–1154. https://doi.org/10.1111/j.1365-3091.2004.00665.x

Holz, C., Stuut, J. B. W., Henrich, R., & Meggers, H. (2007). Variability in terrigenous sedimentation processes off northwest Africa and its relation to climate changes: Inferences from grain-size distributions of a Holocene marine sediment record. *Sedimentary Geology*, *202*(3), 499–508. https://doi.org/10.1016/j.sedgeo.2007.03.015

Jolly, D., Prentice, I. C., Bonnefille, R., Ballouche, A., Bengo, M., Brenac, P., … Waller, M. (1998). Biome reconstruction from pollen and plant macrofossil data for Africa and the Arabian peninsula at 0 and 6000 years. *Journal of Biogeography*, *25*(6), 1007–1027. https://doi.org/10.1046/j.1365-2699.1998.00238.x

Kuechler, R. R., Schefuß, E., Beckmann, B., Dupont, L., & Wefer, G. (2013). NW African hydrology and vegetation during the Last Glacial cycle reflected in plant-wax-specific hydrogen and carbon isotopes. *Quaternary Science Reviews*, *82*, 56–67. https://doi.org/10.1016/j.quascirev.2013.10.013

Kuper, R., & Kröpelin, S. (2006). Climate-controlled Holocene occupation in the Sahara: Motor of Africa's evolution. *Science*, *313*(5788), 803–807.

Kutzbach, J. E. (1981). Monsoon climate of the early Holocene: climate experiment with the

Earth's orbital parameters for 9000 years ago. *Science*, *214*(OCTOBER), 59–61.

Laskar, J., Robutel, P., Joutel, F., Gastineau, M., Correia, A. C. M., & Levrard, B. (2004). Long-term solution for the insolation quantities of the Earth. *Astronomy and Astrophysics*, (428), 261–285. https://doi.org/10.1017/S1743921307011404

Liu, Y., Chiang, J. C. H., Chou, C., & Patricola, C. M. (2014). Atmospheric teleconnection mechanisms of extratropical North Atlantic SST influence on Sahel rainfall. *Climate Dynamics*, *43*(9–10), 2797–2811. https://doi.org/10.1007/s00382-014-2094-8

Locarnini, R. A., Mishonov, A. V., Baranova, O. K., Boyer, T. P., Zweng, M. M., Garcia, H. E., … Smolyar, I. V. (2019). World Ocean Atlas 2018, Volume 1: Temperature. *A. Mishonov, Technical Editor. NOAA Atlas NESDIS*, *1*(81), 52pp.

Mantsis, D. F., Lintner, B. R., Broccoli, A. J., Erb, M. P., Clement, A. C., & Park, H. S. (2014). The response of large-scale circulation to obliquity-induced changes in meridional heating gradients. *Journal of Climate*, *27*(14), 5504–5516. https://doi.org/10.1175/JCLI-D-13-00526.1

Martrat, B., Grimalt, J. O., Shackleton, N. J., De Abreu, L., Hutterli, M. A., & Stocker, T. F. (2007). Four climate cycles of recurring deep and surface water destabilizations on the Iberian margin. *Science*, *317*(5837), 502–507. https://doi.org/10.1126/science.1139994

McGee, D., & deMenocal, P. B. (2017). *Climatic Changes and Cultural Responses During the African Humid Period Recorded in Multi-Proxy Data* (Vol. 1). Oxford University Press. https://doi.org/10.1093/acrefore/9780190228620.013.529

McGee, D., DeMenocal, P. B., Winckler, G., Stuut, J. B. W., & Bradtmiller, L. I. (2013). The magnitude, timing and abruptness of changes in North African dust deposition over the last 20,000yr. *Earth and Planetary Science Letters*, *371–372*, 163–176. https://doi.org/10.1016/j.epsl.2013.03.054

McGee, D., Marcantonio, F., McManus, J. F., & Winckler, G. (2010). The response of excess 230Th and extraterrestrial 3He to sediment redistribution at the Blake Ridge, western North Atlantic. *Earth and Planetary Science Letters*, *299*(1–2), 138–149. https://doi.org/10.1016/j.epsl.2010.08.029

McGee, D., Moreno-Chamarro, E., Green, B., Marshall, J., Galbraith, E., & Bradtmiller, L. (2018). Hemispherically asymmetric trade wind changes as signatures of past ITCZ shifts. *Quaternary Science Reviews*, *180*, 214–228.

https://doi.org/10.1016/j.quascirev.2017.11.020

Meyer, I., Davies, G. R., Vogt, C., Kuhlmann, H., & Stuut, J. B. W. (2013). Changing rainfall patterns in NW Africa since the Younger Dryas. *Aeolian Research*, *10*, 111–123. https://doi.org/10.1016/j.aeolia.2013.03.003

Middleton, J. L., Mukhopadhyay, S., Langmuir, C. H., McManus, J. F., & Huybers, P. J. (2018). Millennial-scale variations in dustiness recorded in Mid-Atlantic sediments from 0 to 70 ka. *Earth and Planetary Science Letters*, *482*, 12–22. https://doi.org/10.1016/j.epsl.2017.10.034

Mortlock, R. A., & Froelich, P. N. (1989). A simple method for the rapid determination of biogenic opal in pelagic marine sediments. *Deep Sea Research Part A, Oceanographic Research Papers*, *36*(9), 1415–1426. https://doi.org/10.1016/0198-0149(89)90092-7

Mulitza, S., Heslop, D., Pittauerova, D., Fischer, H. W., Meyer, I., Stuut, J. B., … Schulz, M. (2010). Increase in African dust flux at the onset of commercial agriculture in the Sahel region. *Nature*, *466*(7303), 226–228. https://doi.org/10.1038/nature09213

Mulitza, S., Prange, M., Stuut, J. B., Zabel, M., Von Dobeneck, T., Itambi, A. C., … Wefer, G. (2008). Sahel megadroughts triggered by glacial slowdowns of Atlantic meridional overturning. *Paleoceanography*, *23*(4), 1–11. https://doi.org/10.1029/2008PA001637

Murphy, L. N., Clement, A. C., Albani, S., Mahowald, N. M., Swart, P., & Arienzo, M. M. (2014). Simulated changes in atmospheric dust in response to a Heinrich stadial. *Paleoceanography*, *29*(1), 30–43. https://doi.org/10.1002/2013PA002550

Ndeye, M. (2008). Marine reservoir ages in northern Senegal and Mauritania coastal waters. *Radiocarbon*, *50*(2), 281–288. https://doi.org/10.1017/S0033822200033580

Pittauerov, D., Mulitza, S., Hettwig, B., Chehade, W., Stuut, J.-B., Mollenhauer, G., & Fischer, H. W. (2009). Application of self-absorption correction method in gamma spectroscopy for 210 Pb and 137 Cs sediment chronology on the continental slope off NW Africa . *Radioprotection*, *44*(5), 457–461. https://doi.org/10.1051/radiopro/20095085

Prospero, J. M., & Lamb, P. J. (2003). African droughts and dust trasport to the Caribbean: climate change implications. *Science*, *302*(5647), 1024–1027. https://doi.org/10.1126/science.1089915

Rasmussen, S. O., Andersen, K. K., Svensson, A. M., Steffensen, J. P., Vinther, B. M., Clausen, H. B., … Ruth, U. (2006). A new Greenland ice core chronology for the last glacial termination. *Journal of Geophysical Research*, *111*, 1–16.

https://doi.org/10.1029/2005JD006079

Ratmeyer, V., Balzer, W., Bergametti, G., Chiapello, I., Fischer, G., & Wyputta, U. (1999). Seasonal impact of mineral dust on deep-ocean particle flux in the eastern subtropical Atlantic Ocean. *Marine Geology*, *159*, 241–252.

Reimer, P. J., Bard, E., Bayliss, A., Beck, J. W., Blackwell, P. G., Ramsey, C. B., … van der Plicht, J. (2013). IntCal13 and Marine13 Radiocarbon Age Calibration Curves 0–50,000 Years cal BP. *Radiocarbon*, *55*(04), 1869–1887. https://doi.org/10.2458/azu_js_rc.55.16947

Ridley, D. A., Heald, C. L., & Ford, B. (2012). North African dust export and deposition: A satellite and model perspective. *Journal of Geophysical Research Atmospheres*, *117*(2), 1–21. https://doi.org/10.1029/2011JD016794

Ridley, D. A., Heald, C. L., & Prospero, J. M. (2014). What controls the recent changes in African mineral dust aerosol across the Atlantic? *Atmospheric Chemistry and Physics*, *14*(11), 5735–5747. https://doi.org/10.5194/acp-14-5735-2014

Romero, O. E., Kim, J. H., & Donner, B. (2008). Submillennial-to-millennial variability of diatom production off Mauritania, NW Africa, during the last glacial cycle. *Paleoceanography*, *23*(3), 1–17. https://doi.org/10.1029/2008PA001601

Ruddiman, W., Sarnthein, M., Baldauf, J., Backman, J., Bloemendal, J., Curry, W., … Yasuda, H. (1988). *Proceedings of the Ocean Drilling Program Leg 108*.

Sánchez Goñi, M. F., & Harrison, S. P. (2010). Millennial-scale climate variability and vegetation changes during the Last Glacial: Concepts and terminology. *Quaternary Science Reviews*, *29*(21–22), 2823–2827. https://doi.org/10.1016/j.quascirev.2009.11.014

Scheuvens, D., Schütz, L., Kandler, K., Ebert, M., & Weinbruch, S. (2013). Earth-Science Reviews Bulk composition of northern African dust and its source sediments — A compilation. *Earth Science Reviews*, *116*, 170–194. https://doi.org/10.1016/j.earscirev.2012.08.005

Seierstad, I. K., Abbott, P. M., Bigler, M., Blunier, T., Bourne, A. J., Brook, E., … Vinther, B. M. (2014). Consistently dated records from the Greenland GRIP, GISP2 and NGRIP ice cores for the past 104ka reveal regional millennial-scale δ18O gradients with possible Heinrich event imprint. *Quaternary Science Reviews*, *106*, 29–46. https://doi.org/10.1016/j.quascirev.2014.10.032

Singarayer, J. S., Valdes, P. J., & Roberts, W. H. G. (2017). Ocean dominated expansion and

908 contraction of the late Quaternary tropical rainbelt. *Scientific Reports*, *7*(1), 1–9.
909 https://doi.org/10.1038/s41598-017-09816-8
910 Skonieczny, C., Bory, A., Bout-Roumazeilles, V., Abouchami, W., Galer, S. J. G., Crosta, X., …
911 Ndiaye, T. (2013). A three-year time series of mineral dust deposits on the West African
912 margin : Sedimentological and geochemical signatures and implications for interpretation of
913 marine paleo-dust records. *Earth and Planetary Science Letters*, *364*, 145–156.
914 https://doi.org/10.1016/j.epsl.2012.12.039
915 Skonieczny, C., McGee, D., Winckler, G., Bory, A., Bradtmiller, L. I., Kinsley, C. W., …
916 Malaizé, B. (2019). Monsoon-driven Saharan dust variability over the past 240,000 years.
917 *Science Advances*, *5*(1), eaav1887. https://doi.org/10.1126/sciadv.aav1887
918 Skonieczny, C., Paillou, P., Bory, A., Bayon, G., Biscara, L., Crosta, X., … Grousset, F. (2015).
919 African humid periods triggered the reactivation of a large river system in Western Sahara.
920 *Nature Communications*, *6*, 6–11. https://doi.org/10.1038/ncomms9751
921 Stuut, J. B., Zabel, M., Ratmeyer, V., Helmke, P., Schefuß, E., Lavik, G., & Schneider, R.
922 (2005). Provenance of present-day eolian dust collected off NW Africa. *Journal of*
923 *Geophysical Research: Atmospheres*, *110*(4), 1–14. https://doi.org/10.1029/2004JD005161
924 Suman, D. O., & Bacon, M. P. (1989). Variations in Holocene sedimentation in the North
925 American Basin determined from230Th measurements. *Deep Sea Research Part A,*
926 *Oceanographic Research Papers*, *36*(6), 869–878. https://doi.org/10.1016/0198-
927 0149(89)90033-2
928 Sun, D. (2004). Monsoon and westerly circulation changes recorded in the late Cenozoic aeolian
929 sequences of Northern China. *Global and Planetary Change*, *41*(1), 63–80.
930 https://doi.org/10.1016/j.gloplacha.2003.11.001
931 Tierney, J. E., deMenocal, P. B., & Zander, P. D. (2017). A climatic context for the out-of-Africa
932 migration. *Geology*, *45*(11), 1023–1026. https://doi.org/10.1130/G39457.1
933 Tierney, J. E., Pausata, F. S. R., & De Menocal, P. B. (2017). Rainfall regimes of the Green
934 Sahara. *Science Advances*, *3*(1), 1–10. https://doi.org/10.1126/sciadv.1601503
935 Tjallingii, R., Claussen, M., Stuut, J. B. W., Fohlmeister, J., Jahn, A., Bickert, T., … Röhl, U.
936 (2008). Coherent high- and low-latitude control of the northwest African hydrological
937 balance. *Nature Geoscience*, *1*(10), 670–675. https://doi.org/10.1038/ngeo289
938 van der Does, M., Korte, L. F., Munday, C. I., Brummer, G. J. A., & Stuut, J. B. W. (2016).

Particle size traces modern Saharan dust transport and deposition across the equatorial North Atlantic. *Atmospheric Chemistry and Physics*, *16*(21), 13697–13710. https://doi.org/10.5194/acp-16-13697-2016

van der Jagt, H., Friese, C., Stuut, J.-B. W., Fischer, G., & Iversen, M. H. (2018). The ballasting effect of Saharan dust deposition on aggregate dynamics and carbon export: Aggregation, settling, and scavenging potential of marine snow. *Limnology and Oceanography*, *63*, 1386–1394. https://doi.org/10.1002/lno.10779

Waelbroeck, C., Labeyrie, L., Michel, E., Duplessy, J. C., McManus, J. F., Lambeck, K., … Labracherie, M. (2002). Sea-level and deep water temperature changes derived from benthic foraminifera isotopic records. *Quaternary Science Reviews*, *21*(1–3), 295–305. https://doi.org/10.1016/S0277-3791(01)00101-9

Waelbroeck, C., Paul, A., Kucera, M., Rosell-Melé, A., Weinelt, M., Schneider, R., … Turon, J. L. (2009). Constraints on the magnitude and patterns of ocean cooling at the Last Glacial Maximum. *Nature Geoscience*, *2*(2), 127–132. https://doi.org/10.1038/ngeo411

Wang, W., Evan, A. T., Flamant, C., & Lavaysse, C. (2015). On the decadal scale correlation between African dust and Sahel rainfall: The role of Saharan heat low-forced winds. *Science Advances*, *1*(9), 2010–2015. https://doi.org/10.1126/sciadv.1500646

Weldeab, S., Lea, D. W., Schneider, R. R., & Andersen, N. (2007). 55,000 Years of West African Monsoon and Ocean Thermal Evolution. *Science*, *316*(June), 1303–1306.

Weldeab, S., Menke, V., & Schmiedl, G. (2014). The pace of East African monsoon evolution during the Holocene. *Geophysical Research Letters*, (41), 1724–1731. https://doi.org/10.1002/2014GL059361

Williams, R. H., McGee, D., Kinsley, C. W., Ridley, D. A., Hu, S., Fedorov, A., … deMenocal, P. B. (2016). Glacial to Holocene changes in trans-Atlantic Saharan dust transport and dust-climate feedbacks. *Science Advances*, *2*(11), 1–12. https://doi.org/10.1126/sciadv.1600445

Yu, H., Chin, M., Bian, H., Yuan, T., Prospero, J. M., Omar, A. H., … Zhang, Z. (2015). Remote Sensing of Environment Quanti fi cation of trans-Atlantic dust transport from seven-year (2007 – 2013) record of CALIPSO lidar measurements. *Remote Sensing of Environment*, *159*, 232–249. https://doi.org/10.1016/j.rse.2014.12.010

Zobeck, T. M., Gill, T. E., & Popham, T. W. (1999). A two-parameter Weibull function to describe airborne dust particle size distributions. *Earth Surface Processes and Landforms*,

970 *955*, 943–955. https://doi.org/10.1002/(SICI)1096-9837(199909)24:10<943::AID-
971 ESP30>3.0.CO;2-9
972